Winter 2012

Perpendicular Ion Heating by Low-frequency Alfven-wave Turbulence

Qian Xia
University of New Hampshire, Durham

Perpendicular Ion Heating by Low-frequency Alfvén-wave Turbulence

BY

Qian Xia

Submitted to the University of New Hampshire
in partial fulfillment of
the requirements for the degree of

Doctor of Philosophy

in

Phyics

Dec 2012

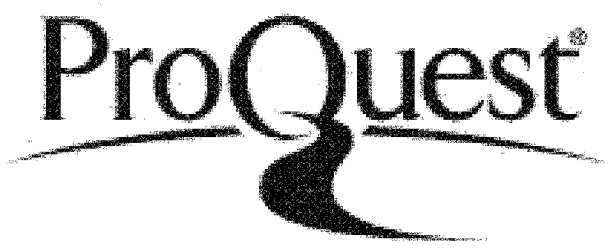

ProQuest LLC
789 East Eisenhower Parkway
P.O. Box 1346
Ann Arbor, MI 48106-1346

This dissertation has been examined and approved.

Disertation Director, Benjamin G.D Chandran
Professor, Department of Physics

Silas R. Beane
Associate Professor, Department of Physics

Kai Germaschewski
Assistant Professor, Department of Physics

Martin Lee
Professor, Department of Physics

Phil Isenberg
Research Professor, Department of Physics

10/2/12
Date

ACKNOWLEDGMENTS

A number of people have made this dissertation possible. I wish to thank my committee members: Silas R. Beane, Kai Germaschewski, Martin Lee, Phil Isenberg for their suggestions.

This thesis includes many numerical simulations, which were carried out on the cluster Zaphod at UNH, Plasma01 at University of Wisconsin at Madison, the supercomputer Ranger from Texas Advanced Computing Center (TACC), and Kraken from National Institute for Computational Sciences (NICS). Prof. Chung-Sang Ng also helped me a lot on my turbulence simulation study in UNH.

In particular, I wish to thank my advisor, Prof. Benjamin G.D Chandran, and Dr. Jean Carlos Perez for their great guidance, knowledge and wisdom.

Finally I would like to express my gratitude to my family for their support and encouragement.

TABLE OF CONTENTS

LIST OF TABLES

LIST OF FIGURES

ABSTRACT

Perpendicular Ion Heating by Low-frequency Alfvén-wave Turbulence

by

Qian Xia

University of New Hampshire, Dec. 2012

Determining the mechanisms that heat the solar corona is a fundamental problem in heliospheric physics. One of the proposed models is based on low-frequency Alfvén waves ($\omega \ll \Omega_i$) launched from the coronal base. Theoretical studies and numerical simulations have shown that Alfvén-wave low-β turbulence primarily cascades to smaller scales perpendicular to the mean magnetic field rather than smaller parallel scales, where $\beta = 8\pi p/B^2$ is the ratio of the plasma pressure to the magnetic pressure. Because of this, the wave frequencies at small scales remain small compared to the proton cyclotron frequency. In this work, we study the possibility of ion heating by this low-frequency Alfvén-wave turbulence in a reduced magnetohydrodynamic (RMHD) simulation. In a low-β plasma, when an ion's gyroradius is comparable to the wave length in the perpendicular direction, the ion undergoes a random walk in the time-varying electrostatic potential. When the fluctuation amplitude exceeds a certain threshold, this stochastic mechanism provides ion heating in the plane perpendicular to the magnetic field lines. We evaluate the stochastic heating rate as a function of the amplitude of the turbulence and compare our findings to previous theoretical results.

CHAPTER 1

INTRODUCTION

1.1 The Solar Wind

The ionized plasma that comes from the Sun and spreads over the whole heliosphere is called the solar wind. It consists mainly of electrons and protons along with α particles (about 10% of the mass), and a tiny fraction of heavy ions ($\leq 1\%$) (*Bame et al.*, 1977). In the 1960s, Parker found that the solar wind is faster and hotter than the theoretical result based on a hydrodynamic model with thermal conduction. The solar convection zone has more than enough energy to drive the solar wind (*McIntosh et al.*, 2007). The mechanism(s) that transfer this mechanical energy to thermal energy and bulk-flow kinetic energy of the ejected plasma is still a mystery. The temperature above the photosphere dramatically increases from $\sim 6 \times 10^3$K to $\sim 10^6$K in short distance, $\sim 10^4$km, above the photosphere (see appendix A.1).

To start with this puzzle, we need to distinguish two types of solar wind: fast wind ($\sim$ 750 km/s) and slow wind ($\sim$ 400 km/s). The fast wind comes from coronal holes where the magnetic field lines are "open", connecting the Sun to the distant heliosphere (*Miralles et al.*, 2002, 2004). The source regions of the slow solar wind have not been unambiguously identified. Possibilities include the streamer belt, closed magnetic loops, and open fields with a large expansion factor (*Wang and Sheeley*, 1990). Near solar minimum, the fast wind fills most of the heliosphere, except for a slow-solar-wind region at small heliographic latitude ($\leq 15^o$). Near solar maximum, fast and slow wind can both be found at virtually all heliographic latitudes (*McComas*

et al., 2003). It is not clear whether fast wind and slow wind have the same origin. From observations, we know that the fast wind has fewer structures and is steadier than the slow wind. The fast wind also has more power in waves and turbulence (*Tu and Marsch*, 1995). All of this makes fast wind a good starting point for studying the physics behind the solar wind, such as the processes that heat the corona to $\sim 10^6$K and accelerate the solar wind to supersonic and super-Alfvénic speeds.

The accelerated particles in the solar wind also have very distinct features constraining the heating mechanisms. In situ measurements in the low-β solar wind found that the proton core temperature perpendicular to the magnetic field is higher than the proton temperature parallel to the magnetic field ($T_\perp > T_\parallel$) (*Marsch et al.*, 1982b, 2004; *Hellinger et al.*, 2006). This suggests the heating mechanism is able to heat the particles preferentially perpendicular to the magnetic field. The Ultraviolet Coronagraph Spectrometer (UVCS) on board the Solar and Heliospheric Observatory (SOHO) satellite found that the temperature of heavy ions is larger than the proton temperature in the north polar coronal hole, and also anisotropic (*Kohl et al.*, 1997; *Esser et al.*, 1999). The kinetic ion temperatures in these papers are calculated from the measurements of remotely observed spectral line widths (Lyα λ1216, Mg x λ625, O VI λ1038). Oxygen O^{+5} and Magnesium Mg^{+9} are strongly heated between $1.3R_s - 2.0R_s$. The minor ions are also heated anisotropically, with $T_\perp \gg T_\parallel$ (*Kohl, J., et al.*, 1998; *Li et al.*, 1998; *Antonucci et al.*, 2000).

1.2 Models for the Origin of the Solar Wind

Some solar-wind models investigated particle kinetic behavior in the solar gravitational potential field (*Lemaire and Scherer*, 1971; *Scudder*, 1992a,b), or instabilities driven by electron beams (*Markovskii and Hollweg*, 2002; *Markovskii et al.*, 2006).

Other studies focus on interchange reconnection (*Fisk*, 2003; *Schwadron and McComas*, 2003), or waves and turbulence (*Hollweg*, 1986; *Velli et al.*, 1989; *Matthaeus et al.*, 1999; *Cranmer and van Ballegooijen*, 2005; *Cranmer et al.*, 2007; *Verdini and Velli*, 2007). In this work, we focus on wave-turbulence (WT) models.

WT models suggest that photospheric motions launch waves (mostly Alfvén waves) that propagate outward and get partially reflected due to gradients in the Alfvén speed. The coupling between oppositely propagating Alfvén waves develops magnetohydrodynamic (MHD) turbulence, which causes large-scale kinetic/magnetic energy to cascade to smaller and smaller scales. At sufficiently small scales the fluctuations strongly interact with particles, heating the plasma and dissipating the turbulence (*Cranmer and van Ballegooijen*, 2003; *Chandran*, 2005).

WT models are supported by a number of observations. For example, in the 1970s, Mariner 5 in situ observations found that the fluctuating fluid velocity $\delta\mathbf{u}$ and magnetic field $\delta\mathbf{B}$ often satisfy the relation $\delta\mathbf{u} = \pm\delta\mathbf{B}/\sqrt{4\pi\rho}$ (where ρ is the plasma density), consistent with Alfvén waves propagating away from the Sun in the solar-wind frame (*Belcher and Davis*, 1971). The fact that the fractional density fluctuation amplitude $\delta\rho/\rho_0$ is much smaller than the fractional magnetic field fluctuation, $|\delta\mathbf{B}|/B$, rules out the possibility that magnetosonic waves account for most of the velocity and magnetic-field fluctuations (*Belcher and Davis*, 1971). Recently, high-resolution remote observations of open magnetic field lines above the photosphere found that Alfvén waves have enough power to drive the solar wind (*De Pontieu et al.*, 2007). These observations determined the Alfvén wave energy flux by measuring the horizontal motion of the magnetic lines in the low corona. The amplitudes of Alfvén waves in the solar wind correlate strongly with temperature, suggesting a connection between Alfvén waves and particle heating (*Grappin et al.*, 1990).

In the past decades, WT models explored the possibility of a mechanism called cyclotron resonance. For it to occur, the wave and particle must satisfy the resonance condition $\omega - k_\parallel v_\parallel = n\Omega_i$, where ω is the wave frequency, $k_\parallel$ ($v_\parallel$) is the component of the wavevector (particle velocity) along the background magnetic field $\mathbf{B}_0$, Ω_i is the particle gyrofrequency, and n is any integer. When this condition is satisfied, particles can be heated in the direction perpendicular to $\mathbf{B}_0$ - i.e., their perpendicular temperature can increase. However, in this work, we focus on the case in which the wave frequencies are too small for this resonance condition to be satisfied.

Our motivation for focusing on the low-frequency case comes from studies of Alfvén-wave turbulence, which show that energy cascades primarily to low-β small scales measured perpendicular to $\mathbf{B}_0$ rather than small scales parallel to $\mathbf{B}_0$ (*Shebalin et al.*, 1983; *Goldreich and Sridhar*, 1995). As a result, the cascade is ineffective at generating waves with large $k_\parallel$, see Figure (1-1). Because the Alfvén-wave frequency is $\omega = k_\parallel V_A$, the lack of large-$k_\parallel$ waves means that the wave frequencies remain comparatively small - in particular, much smaller than the proton cyclotron frequency (*Quataert*, 1998; *Cranmer and van Ballegooijen*, 2003).

McChesney et al. (1987), *Johnson and Cheng* (2001), and *Chen et al.* (2001) proposed a mechanism called stochastic heating, in which Alfvén waves (or kinetic Alfvén waves) at frequencies $\ll \Omega_i$ can cause perpendicular ion heating. More recently, *Chandran et al.* (2010) developed a theory that quantifies the stochastic heating rate as a function of the amplitude of the turbulence. (These studies are described further in Ch. 3.) In this work, we will revisit these studies and calculate the stochastic heating rate using simulations of test particles propagating in electromagnetic fluctuations obtained from direct numerical simulations of Alfvén wave turbulence.

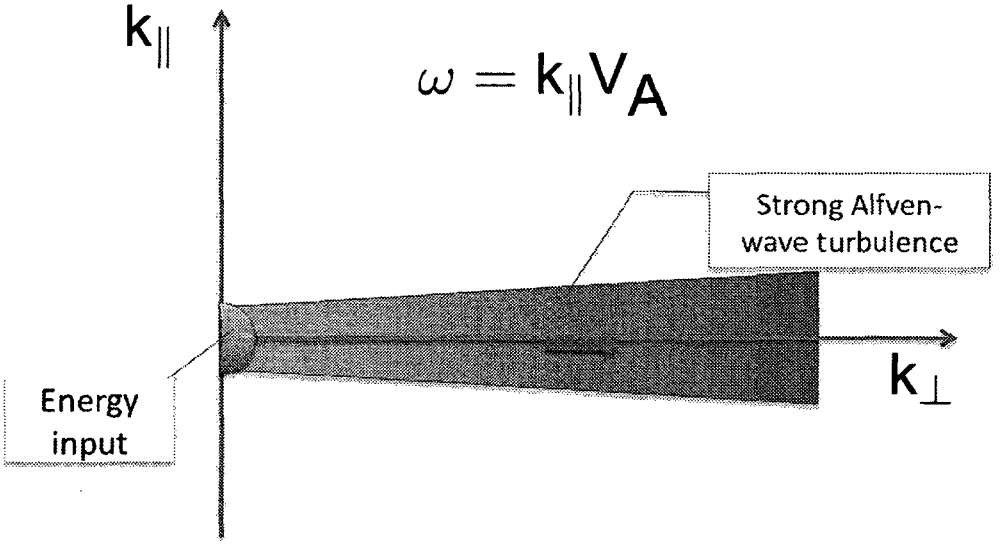

Figure 1-1. Alfvén-wave turbulence energy cascade in wavenumber space

The $k_{\perp}$ ($k_{\|}$) is the wave vector perpendicular (parallel) to the mean magnetic field.

CHAPTER 2

ALFVÉN-WAVE TURBULENCE

2.1 Kolmogorov Dimensional Analysis

Kolmogorov (1941) suggested a theory of hydrodynamic turbulence with the following assumptions:

- Spatial homogeneity
- Isotropy
- Local interactions - large-scale eddies do not distort small-scale eddies, but advect them. The nonlinear interactions are local in scale.

Defining a typical scale length l and the corresponding fluctuation velocity difference δu_l over the scale l, the energy per unit mass of eddies of size l is δu_l^2, and the cascade time (the length of time for the energy to pass to a smaller scale) is $\tau_l \sim l/\delta u_l$. If it is assumed that the inertial range scales have the same physics and are similar to each other, then the power of the cascade is

$$\epsilon \sim \frac{\delta u_l^2}{\tau_l} \sim \frac{\delta u_l^3}{l}. \tag{2.1}$$

implying that $\delta u_l \sim (\epsilon l)^{1/3}$.

The energy will be transferred to increasingly smaller scales until it is dissipated. The viscous dissipation rate is $P_d = \nu u^2/l^2$. In stationary turbulence, $\epsilon = P_d$. ϵ is determined by the driving scale L. One can estimate a dissipation scale l_ν where the

cascade power equals the dissipation rate: $l_\nu \sim (\nu^3/\epsilon)^{1/4}$. At scales $l_\nu \ll l \ll L$ (the inertial range), the energy transport from large scales to small scales is controlled by neither the driving force nor the dissipation mechanisms. The 1D energy spectrum has the relation

$$\delta u_l^2 = kE(k) \Rightarrow E(k) \sim \epsilon^{2/3} k^{-5/3}, \tag{2.2}$$

where $E(k)$ is the energy spectrum and $k \sim 1/l$ is the wave vector.

2.2 Alfvén Waves

A useful approximation for large-scale, low-frequency phenomena in plasmas is the MHD model, which treats a plasma as a single, electrically neutral, conducting fluid. In MHD, the plasma is described by the following equations,

1. Mass conservation:

$$\frac{\partial \rho}{\partial t} + \nabla \cdot (\rho \mathbf{u}) = 0 \tag{2.3}$$

2. Faraday's law:

$$\nabla \times \mathbf{E} = -\frac{1}{c} \cdot \frac{\partial \mathbf{B}}{\partial t} \tag{2.4}$$

where $\mathbf{E}$ is the electric field.

3. Amperè's law, neglecting the displacement current:

$$\nabla \times \mathbf{B} = \frac{4\pi}{c} \mathbf{J} \tag{2.5}$$

where $\mathbf{J}$ is the current density.

4. Ohm's law:

$$\mathbf{E} + \frac{1}{c} \mathbf{u} \times \mathbf{B} = \frac{4\pi\eta}{c^2} \mathbf{J} \tag{2.6}$$

where η is the magnetic diffusivity.

5. The equation of motion with isotropic pressure tensor:

$$\rho\left(\frac{\partial \mathbf{u}}{\partial t}+\mathbf{u}\cdot\nabla\mathbf{u}\right)=-\nabla\left(p+\frac{B^2}{8\pi}\right)+\frac{1}{4\pi}\mathbf{B}\cdot\nabla\mathbf{B}+\rho\nu\nabla^2\mathbf{u} \tag{2.7}$$

where ν is the viscosity.

Using Equations (2.4)-(2.6) one finds:

$$\frac{\partial \mathbf{B}}{\partial t}=\nabla\times(\mathbf{u}\times\mathbf{B})+\eta\nabla^2\mathbf{B} \tag{2.8}$$

The equations can be simplified further for our specific problem. The incompressibility condition, ρ = const, or $\nabla\cdot\mathbf{u}=0$ is applied in this paper. We write $\mathbf{B}=\mathbf{B}_0+\delta\mathbf{B}$, where $\mathbf{B}_0$ is the mean field (it is assumed to be along the z axis). Equations (2.7) and (2.8) transform to the Elsässer equations:

$$\frac{\partial \mathbf{z}^{\pm}}{\partial t}\pm(\mathbf{v}_A\cdot\nabla)\mathbf{z}^{\pm}+(\mathbf{z}^{\mp}\cdot\nabla)\mathbf{z}^{\pm}=-\nabla P+\frac{1}{2}(\nu+\eta)\nabla^2\mathbf{z}^{\pm}+\frac{1}{2}(\nu-\eta)\nabla^2\mathbf{z}^{\mp} \tag{2.9}$$

where the Elsässer variables $\mathbf{z}^{\pm}=\mathbf{u}\mp\mathbf{b}$, $\mathbf{b}=\delta\mathbf{B}/\sqrt{4\pi\rho}$, the Alfvén velocity $\mathbf{v}_A=\mathbf{B}_0/\sqrt{4\pi\rho}$, and $P=p/\rho+B^2/8\pi\rho$ is the total pressure density. When $\mathbf{z}^-$ or $\mathbf{z}^+$ equals 0 throughout a finite volume, the non-linear term $(\mathbf{z}^{\mp}\cdot\nabla)\mathbf{z}^{\pm}$ vanishes within that volume. Equation (2.9) has simple solutions of Alfvén waves propagating parallel or anti-parallel to $\mathbf{B}_0$ at speed v_A.

2.3 MHD Turbulence

2.3.1 Iroshnikov - Kraichnan Theory

The difference between hydrodynamic and magnetohydrodynamic problems is the existence of the magnetic field. The non-linear interaction term between $\mathbf{z}^+$ and $\mathbf{z}^-$

demonstrates that collisions between oppositely propagating waves cause the modification of wave packets that produces the turbulent energy cascade.

Iroshnikov (1963) and Kraichnan (1965) followed Kolmogorov's approach to hydrodynamic turbulence by treating Alfvén wave packets as isotropic - i.e., as having comparable dimensions perpendicular and parallel to $\mathbf{B}$. For a wave packet of size l, the characteristic wave-packet correlation length, the Alfvén time, is defined as

$$\tau_A = l/v_A, \tag{2.10}$$

and the eddy time is

$$\tau_{nl} \sim l/\delta u_l \tag{2.11}$$

where δu_l is the rms amplitude of the velocity fluctuation in the wavepacket. When a $\mathbf{z}^+$ wave packet collides with a $\mathbf{z}^-$ wave packet with comparable values of l and u_l, the collision lasts a time $\sim \tau_A$ and changes the value of $\mathbf{z}^\pm$ in the wave packets by an amount,

$$\Delta u \sim \delta u_l \frac{\tau_A}{\tau_l}. \tag{2.12}$$

When $\Delta u \ll \delta u_l$, the wave packets change by a small fraction during one interaction. They can survive for many collisions before being totally distorted. The distortions add up randomly like a random walk and thus the changed amplitude will become comparable to the fluctuation velocity after a certain time t that satisfies the relation

$$\Delta u \sqrt{\frac{t}{\tau_A}} \sim \delta u_l. \tag{2.13}$$

Solving for t, we find that

$$t \sim \frac{\tau_{nl}^2}{\tau_A} \sim \frac{v_A l}{\delta u_l^2}. \tag{2.14}$$

We identify this value of t as the energy cascade time t_{cas} at scale l. Upon writing $\epsilon \sim u_l^2/t_{cas}$ one obtains

$$\delta u_l \sim (\epsilon v_A l)^{1/4}. \tag{2.15}$$

After equating l with $1/k$ and setting $(\delta u_l^2) = kE_k$, one obtains

$$E(k) \sim (\epsilon v_A)^{1/2} k^{-3/2}. \tag{2.16}$$

This is called the Iroshnikov-Kraichnan spectrum (IK) for MHD turbulence (*Iroshnikov*, 1963; *Kraichnan*, 1965).

2.3.2 Weak Turbulence

The presence of the magnetic field plays an important role in MHD turbulence, in that it is easier to interchange or shuffle magnetic field lines than it is to bend them when β is low. A mean field $\mathbf{B}_0$ thus introduces anisotropy, causing correlation lengths in the parallel and perpendicular directions to be different: $l_\parallel \neq l_\perp$. As a result, Equation (2.14) becomes

$$t \sim \frac{\tau_l^2}{\tau_A} \sim \frac{l_\perp^2 v_A}{l_\parallel \delta u_l^2}, \tag{2.17}$$

where we have set $\tau_l = l_\perp/\delta u_l$ and $\tau_A = l_\parallel/v_A$. In weak turbulence, $\tau_A \ll \tau_l$. The dispersion relation for Alfvén waves is

$$\omega^\pm = \pm k_\parallel v_A, \tag{2.18}$$

where $\omega^\pm$ is the frequency of a $\mathbf{z}^\pm$ wave. The resonance conditions for three-wave interactions are

$$\mathbf{k}_3 = \mathbf{k}_1 + \mathbf{k}_2 \Rightarrow k_{3\parallel} = k_{1\parallel} + k_{2\parallel} \tag{2.19}$$

$$\omega_3^{\pm} = \omega_1^{\pm} + \omega_2^{\mp} \Rightarrow k_{3\parallel} = k_{1\parallel} - k_{2\parallel}. \tag{2.20}$$

In Equation (2.20), we have made use of the result that nonlinear interactions arise only among counter-propagating waves, so that one of the three interacting waves must propagate in the opposite direction as the other two. Solving Equations (2.19)-(2.20) leads to $k_{2\parallel} = 0$ and $k_{3\parallel} = k_{1\parallel}$. This means that when energy is transferred from one wave with nonzero $k_\parallel$ to another wave with nonzero $k_\parallel$, the two $k_\parallel$ values must be the same. Hence, energy does not cascade from small $k_\parallel$ to large $k_\parallel$ and $l_\parallel$ can be treated as a constant.

Now, $\delta u_l \sim l_\perp^{1/2}$ from Equation (2.17), and the transverse energy spectrum becomes

$$E(k) \sim k_\perp^{-2}. \tag{2.21}$$

2.3.3 The Goldreich - Sridhar Theory

In 1995, Goldreich and Sridhar (GS) suggested that as energy cascades to smaller scales in weak MHD turbulence, $\tau_l \sim l_\perp^{1/2}$ becomes as small as τ_A at sufficiently small $l_\perp$. Once this happens, the turbulence becomes strong, with $\Delta u \sim \delta u$. Goldreich & Sridhar argued that as energy cascades to even smaller $l_\perp$, $l_\parallel$ changes so as to keep $\Delta u \sim \delta u$. This state, in which

$$\frac{l_\parallel}{v_A} \simeq \frac{l_\perp}{\delta u_l}, \tag{2.22}$$

is referred to as "critical balance". Equation (2.22) substituted into Equation (2.17) leads to

$$\delta u_l \sim (\epsilon l_\perp)^{1/3}. \tag{2.23}$$

as in hydrodynamic turbulence. The velocity power spectrum will then satisfy:

$$E(k_\perp) \sim \epsilon^{2/3} k_\perp^{-5/3}. \tag{2.24}$$

From equations (2.22) and (2.23), the relation between $l_\parallel$ and $l_\perp$ is:

$$l_\parallel \propto l_\perp^{2/3}. \tag{2.25}$$

There is thus some cascade to smaller $l_\parallel$ in the strong-turbulence limit. However, the ratio $l_\parallel/l_\perp \propto l_\perp^{-1/3}$, so that eddies become increasingly anisotropic (in the sense of $l_\parallel \gg l_\perp$) as $l_\perp$ decreases. Thus, even in strong turbulence, energy cascades primarily to smaller perpendicular scales, not smaller parallel scales.

2.3.4 The Characteristic Frequencies in Turbulence

Because of Equation (2.18), we can estimate the characteristic frequency of an Alfvén wave packet of parallel dimension $l_\parallel$ as $v_A/l_\parallel$. Equation (2.25) implies that as $l_\perp$ decreases, $l_\parallel$ decreases to a smaller extent, so that the Alfvén-wave cascade is inefficient at generating high-frequency waves.

At the scales deep in the inertial range or at the dissipation scale, the turbulence is strong. Equation (2.22) for the "critical balance" applies. The "wave" conception does not work appropriately at such small scales. However, as just described, we can estimate the wave frequency as

$$\omega_A = v_A/l_\parallel \sim \delta u_l/l_\perp. \tag{2.26}$$

The particle's gyrofrequency is defined as

$$\Omega_p = \frac{v_T}{\rho}, \tag{2.27}$$

where v_T is the thermal speed and ρ is the gyroradius. The condition of Landau damping,

$$\omega - k_\parallel v_\parallel = 0, \tag{2.28}$$

is not satisfied by protons and Alfvén waves in the low-β limit, since the thermal speed is $\ll \omega/k_\parallel = v_A$ when $\beta \ll 1$. For waves with low frequencies satisfying

$$\omega \ll \Omega_p, \tag{2.29}$$

resonant cyclotron interactions with thermal protons do not arise.

We define

$$\epsilon = \frac{\delta u_\rho}{v_T}, \tag{2.30}$$

where δu_ρ is the value of δu_l at the ion gyroscale ($l_\perp \sim \rho$). Equivalently,

$$\epsilon = \frac{\omega_{nl}}{\Omega_p}, \text{ where } \omega_{nl} = \delta u_l / l_\perp \tag{2.31}$$

or, because of critical balance, $\epsilon \sim \omega_A/\Omega_p$. This important parameter will be discussed in more detail in the next Chapter because of its importance for stochastic heating. In the frequency domain, $\delta u_l/v_T$ represents the ratio of the Alfvén frequency to the particle's gyro frequency. When ϵ approaches 1, ion cyclotron resonance is present. The low-frequency limit corresponds to the case with $\epsilon \ll 1$. Upon defining $l_\parallel = (l_\perp/L_\perp)^{2/3} L_\parallel$, and setting $l_\perp = \rho$, we find that

$$\Omega_p \cdot \tau_A = \frac{v_T}{\rho} \cdot \frac{l_\parallel}{v_A} \sim \frac{v_T}{v_A} \cdot \frac{l_\parallel}{\rho} \propto \beta^{1/2} \cdot \frac{L_\parallel}{L_\perp} \cdot \left(\frac{\rho}{L_\perp}\right)^{-1/3}, \tag{2.32}$$

where $L_\parallel$ and $L_\perp$ are the outer-scale values of $l_\parallel$ and $l_\perp$. Typical parameter values in coronal holes at $r = 2.0 R_s$ are $\beta \simeq 0.004$, $L_\perp \simeq 2 \times 10^4$ km, $L_\parallel \simeq 7 \times 10^4$ km, and $\rho \simeq 0.03$ km (*Spruit*, 1981; *Feldman et al.*, 1997; *Cranmer and van Ballegooijen*, 2005). For these values, Equation (2.32) gives

$$\Omega_p \cdot \tau_A \simeq 193 \gg 1, \tag{2.33}$$

which agrees with the assumption that the Alfvén time is much longer than the proton gyroperiod.

CHAPTER 3

STOCHASTIC HEATING

3.1 The Wave Frequency Near the Particle's Gyroscale

Nonlinear interactions cascade the energy to small scales until it reaches the dissipation scale, at which the terms $\frac{1}{2}(\nu \pm \eta)\nabla^2 \mathbf{z}^{\pm}$ and $(\mathbf{z}^{\mp} \cdot \nabla)\mathbf{z}^{\pm}$ are comparable. The wavenumber corresponding to this scale is called k_d, see Figure (3-1). Observations show that k_d is near the proton gyroscale ρ (*Bale et al.*, 2005). At $k \geq k_d$, the fluctuations dissipate, transferring the cascade power to the particles (i.e., causing turbulent heating). Linear Alfvén wave solutions were already invalid in the inertial range.

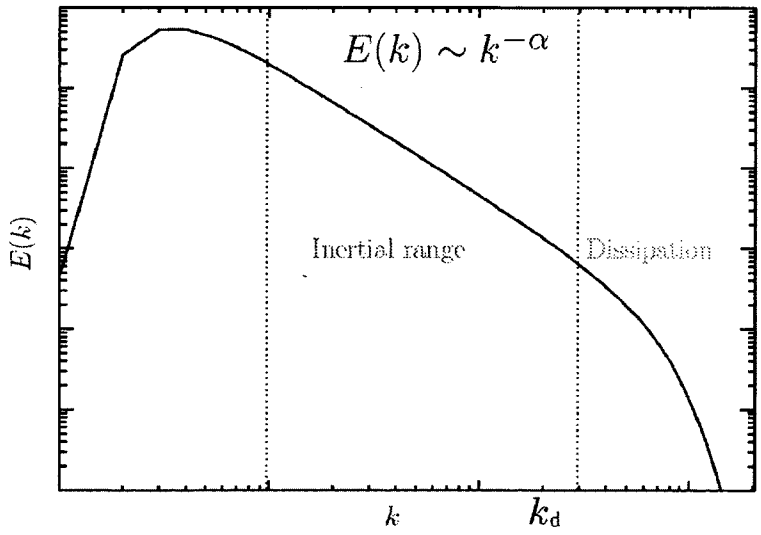

Figure 3-1. Typical turbulence energy spectrum in k space.

At $k_\perp \rho \geq 1$, Alfvén waves become kinetic Alfvén waves (KAW) (*Hollweg*, 1999a; *Howes et al.*, 2008b). Unlike the shear Alfvén wave, the KAW is compressible and

has velocity, electric field and magnetic field fluctuations with nonzero components along the background magnetic field.

Landau damping, transit-time damping, and cyclotron damping are three types of resonant wave-particle interactions that transfer energy between waves and particles. Landau damping and transit-time damping (which is an analogue to Landau damping but with the $\mu\nabla B$ force instead of the electric force) accelerate the particles in the direction parallel to the mean magnetic field $\mathbf{B}_0$. This occurs when a particle's velocity along $\mathbf{B}_0$, given by $v_\parallel$, is equal to the wave phase speed along $\mathbf{B}_0$, which is $\omega/k_\parallel$. For Alfvén waves, this resonance condition is $\omega_A - k_\parallel v_\parallel = 0$. Cyclotron damping requires that $\omega - k_\parallel v_\parallel = n\Omega$, where n is any nonzero integer. In low-β plasmas, $v_\parallel \ll v_A$ for thermal protons. Thus cyclotron damping requires $\omega \simeq n\Omega$ for Alfvén waves interacting with thermal protons when $\beta \ll 1$. For the low frequency AWs and KAWs that we consider, cyclotron damping is absent. Moreover, when $\beta_p \ll 1$, Landau damping and transit-time damping are absent for thermal protons and thermal ions.

3.2 Magnetic Moment Conservation

When a particle moves in a magnetic field, if the fluctuation amplitude is small and/or the wavelength is sufficiently large compared to ρ, its motion is quasi-periodic in the plane perpendicular to $\mathbf{B}_0$. In this case, if the particle interacts with fluctuations with frequencies $\ll \Omega$, then the particle possesses an adiabatic invariant

$$\mu = \frac{mv_\perp^2}{2B}, \tag{3.1}$$

which is the ratio of the particle's transverse kinetic energy to the magnetic field strength (*Kruskal*, 1962). If a particle moves to a location with weaker magnetic field, the particle's perpendicular kinetic energy is transferred to the parallel direction, and μ remains nearly constant.

3.3 Stochastic Ion Heating

When the fluctuation amplitude at $k_\perp \rho \sim 1$ becomes sufficiently large, magnetic moment conservation is lost (*McChesney et al.*, 1987). A particle will gain or lose energy in the electric field of AWs, when the particle moves across an electric-potential structure with a nonzero partial time derivative. For example, if an ion moves through a region in which Φ has a local maximum and $\partial\Phi/\partial t > 0$, then the "potential energy hill" is low when the particle "climbs" the hill and high when the particle rolls down. The particle thus gains extra energy and is accelerated (see Figure 3-2). If $\partial\Phi/\partial t < 0$, the ion will lose energy. Figure (3-3) shows the particle behavior for two different values of ϵ in a test-particle calculation (to be described in more detail in Section 4.4.5). The particle trajectory looks increasingly like a random walk as the fluctuation amplitude becomes larger.

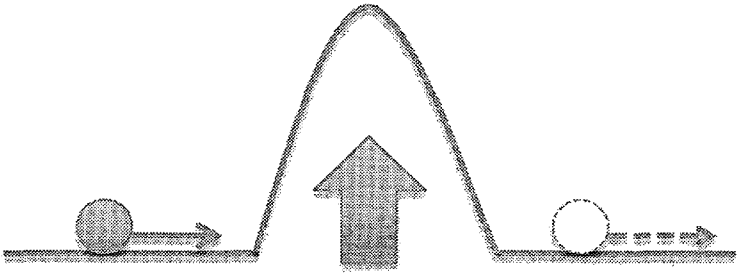

Figure 3-2. A particle gets energy from the increasing electrostatic potential

The ion gyroradius is

$$\rho = \frac{v_\perp}{\Omega_i}, \tag{3.2}$$

where $\Omega = qB_0/mc$ is the ion gyrofrequency, $v_\perp = \sqrt{2k_B T_{\perp i}/m_i}$ is the rms perpendicular velocity of the ion, $T_{\perp i}$ is the perpendicular temperature of the ions, and m_i is the ion mass. The rms amplitude of the fluctuating velocity and magnetic field vectors at the scale $k_\perp \rho \sim 1$ are δu_ρ and δB_ρ. The fluctuating electric field's magnitude is

$$\delta E_\rho \sim \frac{\delta u_\rho B_0}{c}. \tag{3.3}$$

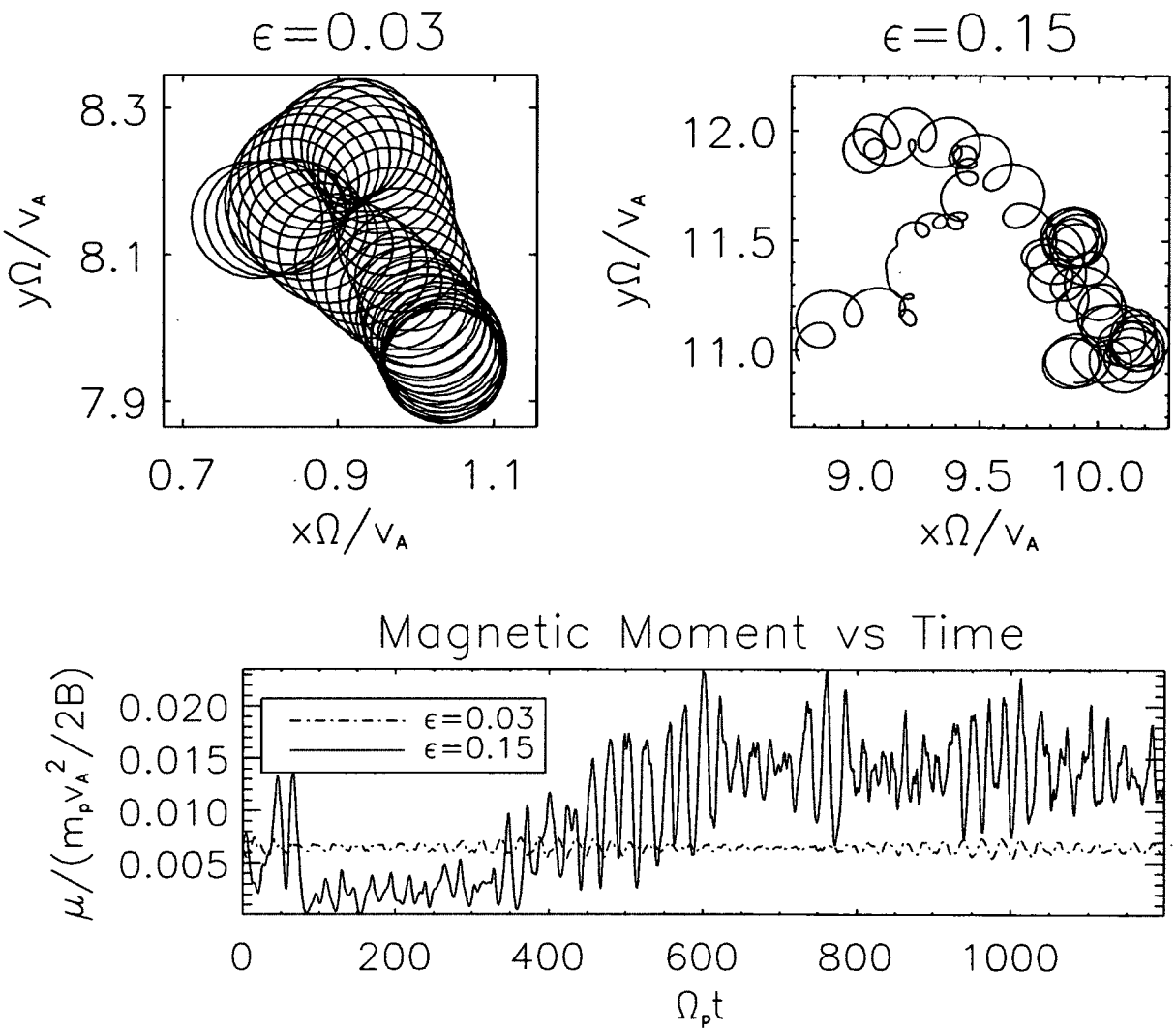

Figure 3-3. Particle drift motion versus fluctuation amplitude

The upper left panel shows a single test particle's trajectory in the plane perpendicular to the background magnetic field, with $\epsilon = 0.03$. The upper right panel is for a particle with $\epsilon = 0.15$. The bottom panel shows the magnetic moment of each particle as a function of time, with the dash-dot line corresponding to $\epsilon = 0.03$ and the solid line corresponding to $\epsilon = 0.15$.

The electrostatic potential energy difference for AWs or for KAWs at $k_\perp \rho \sim 1$ across a distance ρ due to the electric field fluctuations of scale ρ is

$$q\delta\Phi_\rho \simeq q \cdot \rho\delta E_\rho \sim m v_\perp \delta u_\rho. \tag{3.4}$$

The fractional change of the ion's transverse kinetic energy due to moving through a potential-energy difference $q\Phi_\rho$ during a single gyro orbit is

$$\frac{q\delta\Phi_\rho}{\frac{1}{2}mv_\perp^2} \sim \frac{\delta u_\rho}{v_\perp} = \epsilon. \tag{3.5}$$

This ϵ was introduced previously in Chapter 2. When ϵ is sufficiently small, the magnetic moment is conserved almost exactly (*Kruskal*, 1962). As ϵ is increased towards 1, the particle's motion becomes essentially random, and the assumption of quasi-periodic motion in the derivation of μ conservation is violated. In this case, μ conservation is lost, and the particle undergoes a form of heating called "stochastic heating". (*McChesney et al.*, 1987).

3.4 The Heating Rate

Here we consider the Hamiltonian of a particle:

$$H = q\Phi + \frac{1}{2m}\left(\mathbf{p} - \frac{q}{c}\mathbf{A}\right)^2, \tag{3.6}$$

where $\mathbf{p}$ is the canonical momentum, $\mathbf{A}$ is the vector potential, and c is the light speed. The Hamiltonian H is the particle's total energy and its time derivative is

$$\frac{dH}{dt} = q\frac{\partial\Phi}{\partial t} - \frac{q\mathbf{v}}{c} \cdot \frac{\partial\mathbf{A}}{\partial t}. \tag{3.7}$$

The electric field is

$$\mathbf{E} = -\nabla\Phi - \frac{\partial \mathbf{A}}{c\,\partial t}. \tag{3.8}$$

The second term in Equation (3.8) is much smaller than the first one for low-frequency AW/KAWs in low-β plasma in Coulomb gauge ($\nabla \cdot \mathbf{A} = 0$, this electric field has a nonzero curl) (*Hollweg*, 1999b).

We consider only the effects of AW/KAW fluctuations with $k_\perp \rho \sim 1$. When the particle interacts with such waves, its guiding center position

$$\mathbf{R} = \mathbf{r} + \frac{\mathbf{v} \times \hat{\mathbf{b}}}{\Omega} \tag{3.9}$$

moves at a speed $\sim \delta v_\rho$ (*Chandran et al.*, 2010). During a time

$$\Delta t \simeq \frac{\rho}{\delta v_\rho}, \tag{3.10}$$

the particle's guiding center moves a distance $\sim \rho$ and the particle encounters a new set of uncorrelated electromagnetic fields. Here, we have assumed that the AW/KAW fluctuations are "disordered" - either turbulent or a superposition of many randomly phased waves - with a correlation length of $k_\perp^{-1} \sim \rho$ in the plane perpendicular to $\mathbf{B}$. The particle thus undergoes a random walk with a spatial diffusion coefficient of $\sim \rho^2/\Delta t$. The particle also undergoes a random walk in energy. During a time Δt, the particle's perpendicular kinetic energy and Hamiltonian both change by an amount (*Chandran et al.*, 2010)

$$\Delta K_\perp \sim \Delta H \sim q\overline{\frac{\partial \Phi}{\partial t}}\Delta t, \tag{3.11}$$

where $\overline{\partial\Phi/\partial t}$ is the average value of $\partial\Phi/\partial t$ along the particle's orbit during the time interval, which we take to be $\sim \delta\Phi_\rho \cdot \delta u_\rho/\rho$, with $\delta\Phi_\rho$ estimated in Equation (3.4). The

kinetic-energy diffusion coefficient (see Figure 4-5) is then (*Chandran et al.*, 2010)

$$D_K \sim \frac{\Delta K_\perp^2}{\Delta t} \sim m^2 v_\perp^2 \frac{\delta u_\rho^3}{\rho}, \tag{3.12}$$

where we have used

$$\overline{\frac{\partial \Phi}{\partial t}} \sim \frac{\delta u_\rho}{\rho} \delta \Phi. \tag{3.13}$$

The characteristic time for the particle's kinetic energy $K_\perp$ to change by a fraction of order unity is

$$t_H \sim \frac{m^2 v_\perp^4}{D_K}. \tag{3.14}$$

The perpendicular ion heating rate for an ensemble of particles is then given by (*Chandran et al.*, 2010)

$$Q_\perp \sim \frac{v_\perp^2}{\delta t} \sim \frac{\delta u_\rho^3}{\rho}, \tag{3.15}$$

Larger-scale fluctuating electric fields (at $k_\perp \rho \ll 1$) that have low frequency ($\omega \ll \Omega$) sweep the particle with the small-scale fields together. The gyroradius of particles is much smaller than the larger-scale. They produce the drift velocity of particles and do not contribute significantly to stochastic heating. We do not include the effect of magnetic moment conservation in the derivation of Equation (3.15). If $\epsilon \ll 1$, the heating rate is strongly reduced from the original estimate. Because cancellations in the more detailed heating rate should be associated with conservation of μ in the small-ϵ limit (*Chandran et al.*, 2010). Therefore, a multiplicative factor of $\exp(-c_2/\epsilon)$ is added to the right hand side of Equation (3.15). The approximate heating rate function becomes (*Chandran et al.*, 2010):

$$Q_\perp = \frac{c_1 \delta u_\rho^3}{\rho} \exp\left(-\frac{c_2}{\epsilon}\right) \tag{3.16}$$

where c_1 and c_2 are dimensionless constants. The factor of c_1 accounts for uncertainties in the factors of order unity that arise at various steps in the derivation. When

$\epsilon \ll 1$, the heating rate is exponentially sensitive to c_2. If a particle gets heated, $v_\perp$ increases, ϵ decreases. c_2 will determine the heating rate at different solar radius when we try to predict the temperature from this heating rate expression.

3.5 Comparison to Observations

In *Chandran* (2010), this heating rate expression was applied to coronal holes, at heliocentric distances of $1.5 \sim 2.5\ R_s$. The value of δu_ρ was obtained from an observationally constrained turbulence model (*Chandran and Hollweg*, 2009). At $r \geq 2R_s$, thermal conduction and Coulomb collisions have only a small effect on the temperatures of different ion species, and these temperatures are determined by the competing effects of ion heating and cooling resulting from solar-wind expansion. The model of *Chandran* (2010) was able to match the observed ion temperatures provided $c_1 = 1.0$ and $c_2 = 0.15$.

3.6 Previous Test-particle Simulations

Equation (3.16) agrees with the results of test particle simulations with randomly phased Alfvén waves and kinetic Alvén waves whose spectrum is drawn from the critical-balance models of *Goldreich and Sridhar* (1995),and *Cho and Lazarian* (2003). These simulations found that $c_1 = 0.75$ and $c_2 = 0.34$ (*Chandran et al.*, 2010).

However, c_2's value should be smaller in a strong turbulence field. Strong turbulence can not be described as a collection of waves. The set up of randomly phased waves removes information about the coherent structures that arise in turbulence. Much of the cascade power is dissipated in coherent structures in which the fluctuation amplitudes are larger than their rms values (*Dmitruk et al.*, 2004). Near such structures, particle orbits are more stochastic/chaotic than on average, enabling stochastic heating to occur more efficiently. Our goal in this work is to carry out test-

particle simulations of stochastic heating in the electromagnetic fields produced by direct numerical simulations of RMHD turbulence, which contain coherent structures. We describe these simulations in detail in the next Chapter.

CHAPTER 4

TEST-PARTICLE SIMULATION OF STOCHASTIC HEATING BY STRONG AW TURBULENCE

4.1 RMHD Simulations

We use the Reduced MHD (RMHD) code written by Jean C.Perez (*Perez and Boldyrev*, 2008) to provide the turbulent electric and magnetic fields that "push" the test particles. The simulation domain is a 3D box with periodic boundary conditions. The guiding magnetic field, $\mathbf{B}_0$, is along the z axis. The x-y plane is called the perpendicular plane. The perpendicular/parallel directions are according to the mean magnetic field instead of the local magnetic field.

In RMHD, the parallel component of $\mathbf{z}^{\pm}$ in equation (2.9) is ignored. Equation (2.9) becomes the RMHD equation (*Strauss*, 1976; *Schekochihin et al.*, 2009)

$$\frac{\partial \mathbf{z}^{\pm}}{\partial t} \pm \left(\mathbf{v}_A \cdot \nabla_{\parallel}\right) \mathbf{z}^{\pm} + \left(\mathbf{z}^{\mp} \cdot \nabla_{\perp}\right) \mathbf{z}^{\pm} = -\nabla P + \nu \nabla^2 \mathbf{z}^{\pm} + \mathbf{f}^{\pm}, \tag{4.1}$$

where $\mathbf{z}^{\pm}$ is in the x-y plane. The 3rd term $\left(\mathbf{z}^{\mp} \cdot \nabla_{\perp}\right) \mathbf{z}^{\pm}$ on the left-hand side is the non-linear term which cascades the energy to smaller scales. The 3rd term $\mathbf{f}^{\pm}$ on the right-hand side is the set-up driving force which injects AW energy into the simulation at small wavenumbers ($|k| < 3$). The 2nd term on the right is the dissipation term, which damps small-scale fluctuations and prevents the simulation from blowing up. In going from Equation (2.9) to Equation (4.1), we have set $\nu = \eta$. It produces the energy cascade spectrum like Figure (4-1).

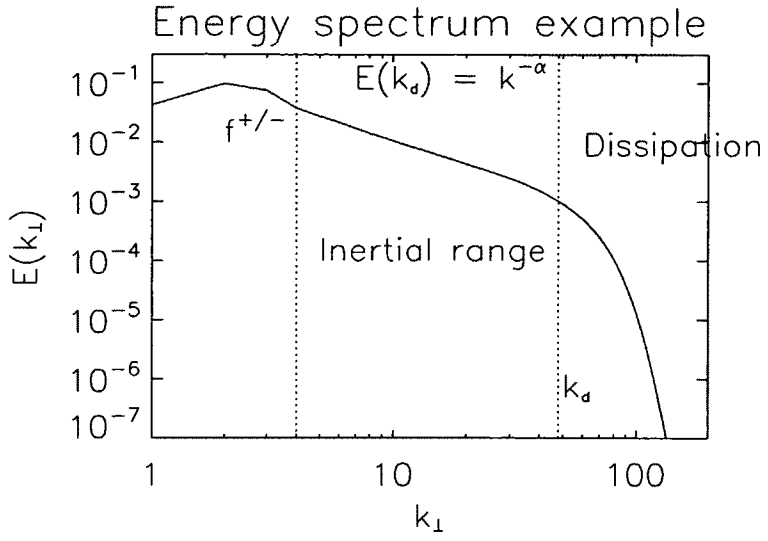

Figure 4-1. The kinetic-energy spectrum in a $512^3 \times 256$ RMHD simulation

The kinetic energy spectrum vs. $k_\perp$ in a 256^3 resolution simulation. The driving force $f^{+/-}$is applied at small $k_\perp$. The dissipation term starts to be dominant at the dissipation wavenumber, k_d.

Since we have taken the flow to be incompressible and in the xy-plane, we can write $\mathbf{u} = -\nabla\phi \times \hat{\mathbf{e}}_z$ and $\mathbf{b} = -\nabla\psi \times \hat{\mathbf{e}}_z$, where $\hat{\mathbf{e}}_z$ is the unit vector along the z axis. Equation (4.1) can be written as two scalar equations:

$$\begin{aligned} \partial_t\omega + (\mathbf{u}\cdot\nabla)\omega - (\mathbf{b}\cdot\nabla)j &= B_0\partial_z j + \nu\nabla^2\omega + f_\omega, \\ \partial_t\psi + (\mathbf{u}\cdot\nabla)\psi &= B_0\partial_z\psi + \eta\nabla^2\phi + f_\phi \end{aligned} \tag{4.2}$$

where $j = \nabla_\perp^2\psi$ is the current density and $\omega = \nabla_\perp^2\psi$ is the vorticity.

The RMHD code solves equation (4.2) using a parallel pseudo-spectral fast Fourier transfer (FFT) method, where the equation is solved in Fourier space, but the non-linear terms are transformed into real space, calculated and transformed back to k-space. This method is used extensively in fluid dynamics because it is fast and highly accurate.

The lengths of the box in the x, y, and z directions are, respectively, $L_\perp, L_\perp$, and $L_\parallel$, with $L_\parallel/L_\perp = v_A/\delta u \times 1.2$, and $L_\perp = 2\pi$, where δu is the rms fluctuating velocity. At the outer scale, the cascade time, or the eddy turn over time, satisfies: $L_\perp/\delta u \leq L_\parallel/v_A$, and the turbulence is strong. The driving force $\mathbf{f}^\pm$ is applied at large scales: $2\pi/L_\perp \leq k_\perp \leq 2(2\pi/L_\perp)$, $2\pi/L_\parallel \leq k_\parallel \leq 2(2\pi/L_\parallel)$.

Each Fourier mode of $\mathbf{f}_n^\pm$ is refreshed to a new random value at time $t_n = n\Delta t_c$ ($n = 0, 1, 2, \ldots$), where the refreshing time is the cascade time Δt_c at the outer scale ($\sim 5L_\perp/v_A$), which is always much larger than the integration time step δt_R of the RMHD code. The code does not use the same $\mathbf{f}_n^\pm$ at each time step $t_m = m\delta t_R$ ($m = 0, 1, 2, \ldots$) before changing. Instead, the next $\mathbf{f}_{n+1}^\pm$ is obtained at $t = t_n$ and the code uses cubic polynomial interpolation to calculate the current $\mathbf{f}_m^\pm$ ($t_n < t_m \leq t_n + \Delta t_c$) from $\mathbf{f}_{n-2}^\pm$, $\mathbf{f}_{n-1}^\pm$,$\mathbf{f}_n^\pm$, and $\mathbf{f}_{n+1}^\pm$, which corresponds to the force at $t_n - 2\Delta t_c$, $t_n - \Delta t_c$, t_n, and $t_n + \Delta t_c$. $\mathbf{f}^\pm$ is continuous and differentiable in time. The amplitudes of the Fourier coefficients of $\mathbf{f}_n^\pm$ are Gaussian random numbers and are chosen so as to keep the fluctuating velocity of order unity.

4.2 Particle Tracing

The test-particle simulations start when the turbulence reaches a statistical steady state, and the damping power (mainly due to dissipation; dealiasing also removes some energy) is equal to the input power from the forcing term f_n. The particle code is parallelized and integrated into the RMHD code (see appendices A.2, and A.4). The number of particles is constant. If a particle leaves one boundary, it re-enters the box from the corresponding point on the opposite boundary (see Figure 4-2).

I neglect Coulomb collisions and track each particle's velocity and position by solving the following equations:

$$\frac{d\mathbf{x}}{dt} = \mathbf{v} \tag{4.3}$$

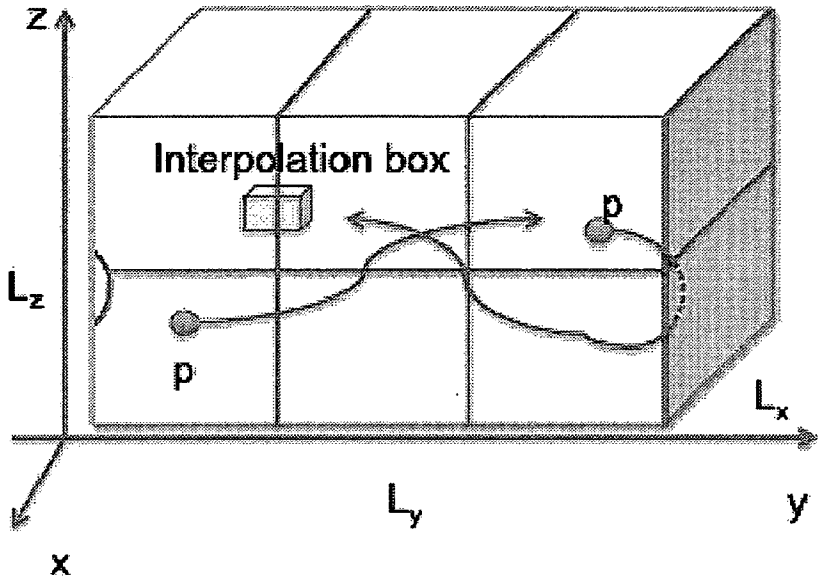

Figure 4-2. Test particles in the simualtion box

The particle does not leave the box. It crosses the boundary and comes back from the opposite wall. The local **E** and **B** are interpolated from a $3 \times 3 \times 3$ grid points around the particle's location. Each point has been interpolated in time first. 6 cubes stand for different domains distributed across the CPU nodes.

and

$$\frac{d\mathbf{v}}{dt} = \frac{q}{m}\left(\mathbf{E} + \frac{\mathbf{v} \times \mathbf{B}}{c}\right), \tag{4.4}$$

where **E** is the electric field, **B** is magnetic field, c is the speed of light, and q and m are the particle's charge and mass.

To study particle heating, we need to track a particle's energy as accurately as possible. Stochastic heating breaks down the particle's adiabatic invariant (magnetic moment), and we want to minimize the risk that the particle integration artificially violates μ conservation through numerical error. We therefore use the Boris pusher (*Boris*, 1970), which differences Equation (4.3) and (4.4) at time $t_i = i\delta t_p$ ($i = 0, 1, 2, \ldots$) using the scheme

$$\frac{\mathbf{x}_{i+1} - \mathbf{x}_i}{\Delta t} = \mathbf{v}_{i+1/2} \tag{4.5}$$

and

$$\frac{\mathbf{v}_{i+1/2} - \mathbf{v}_{i-1/2}}{\Delta t} = \frac{q}{m}\mathbf{E}_i + \frac{q}{mc}\frac{\mathbf{v}_{i+1/2} + \mathbf{v}_{i-1/2}}{2} \times \mathbf{B}_i. \tag{4.6}$$

Equation (4.6) can be re-written as

$$\mathbf{v}^+ - \mathbf{v}^- = (\mathbf{v}^+ + \mathbf{v}^-) \times \frac{\Delta t q}{2mc}\mathbf{B}_i \tag{4.7}$$

with: $\mathbf{v}^{\pm} = \mathbf{v}_{i\pm1/2} \mp \Delta t q/2m\mathbf{E}_i$ (we describe how we choose Δt in appendix A.5.3). In Equation (4.7), $\mathbf{v}^+$ can be obtained from $\mathbf{v}^-$ by 2 rotations along the direction of $\mathbf{B}_i$, so that $|v^+|^2 = |v^-|^2$ to machine precision. The virtue of this approach can be seen by comparing it to a standard Runge-Kutta (RK) discretization. In a constant, uniform magnetic field, fourth-order RK differencing leads to a secular increase in a particle's perpendicular kinetic energy (*Lehe et al.*, 2009). In contrast, under the same conditions, the Boris pusher correctly conserves a particle's perpendicular kinetic energy to machine accuracy. We have tested this method in the same AW/KAW field as *Chandran et al.* (2010) and obtained the same result for c_1, c_2. More details about the Boris pusher will be presented in appendix A.3.

The electric field $\mathbf{E}$ comes from Ohm's Law and Faraday's Law(see the discussion of Equation (10) in *Lehe et al.* (2009))

$$\mathbf{E} = -\frac{\mathbf{u}}{c} \times \mathbf{B} + \eta\mathbf{J}, \tag{4.8}$$

where

$$\mathbf{J} = \frac{c}{4\pi}\nabla \times \mathbf{B}. \tag{4.9}$$

We interpolate the electric and magnetic fields from the grid points to each particle's position. We follow *Lehe et al.* (2009) in using the triangular-shaped cloud (TSC) method to interpolate the field information in 4 dimensions (space and time,

see appendix A.2). To avoid introducing an artificial $\mathbf{E}_{\parallel}$ due to the interpolation method, equation (14) from *Lehe et al.* (2009) is also applied here,

$$\tilde{\mathbf{E}} = \overline{\mathbf{E}} + (\overline{\mathbf{E}\cdot\mathbf{B}} - \overline{\mathbf{E}}\cdot\overline{\mathbf{B}})\frac{\overline{\mathbf{B}}}{||\overline{\mathbf{B}}||^2}. \tag{4.10}$$

Equation (4.10) conserves the electric field along the local magnetic field lines: $\tilde{\mathbf{E}}\cdot\overline{\mathbf{B}} = \overline{\mathbf{E}\cdot\mathbf{B}}$, where the overlines stand for TSC interpolation.

The test particles' velocities are initialized randomly using a Maxwell ion distribution corresponding to the desired value of ϵ. The positions of these are uniformly distributed across the whole box with random positions.

During the first few gyroperiods of each test-particle simulation, the particles pick up the drift velocity of the local large-scale eddies and the temperature increases abruptly. Subsequently, the temperature increases more steadily due to the stochastic heating. However, as time proceeds, ϵ decreases as the temperature increases ($v_\perp \Uparrow$), reducing the heating rate $Q_\perp$ (see Equation 3.16). To calculate $Q_\perp$ (the perpendicular heating rate per unit mass), we set

$$Q_\perp = \frac{1}{2}\left(\frac{< v_{\perp f}^2 > - < v_{\perp 0}^2 >}{t_f - t_0}\right) \tag{4.11}$$

where $< ... >$ indicates an average over all simulated particles, $v_{\perp 0}$ ($v_{\perp f}$) is a particle's perpendicular velocity at $t = t_0$ ($t = t_f$), where $t_0 = 10/\Omega_i$, and t_f is either the end of the simulation, or the time at which $< v_{\perp f}^2 >= 1.2 < v_{\perp 0}^2 >$. The heating rate for a given ϵ is averaged from different simulations with the same original ϵ. The number of test particles in the code is more than 10^5 (see appendix A.5.2).

4.3 The Simulation Resolution and the Spectrum

The box length of $N_\perp^2 \times N_\parallel$ resolution simulation are L_i ($i = 1, 2, 3$ stands for 3 dimensions), giving the integer coordinate components,

$$x_j = \frac{L_i}{N_i} l_j, \ 0 \leq l_j \leq N_i \tag{4.12}$$

where the wave number $k = 2\pi/x$ has the values,

$$k_m = \frac{2\pi}{L_i} s_m, \ -\frac{N_i}{2} \leq s_m \leq \frac{N_i}{2}. \tag{4.13}$$

When $L_i = 2\pi$, for example, $|k_m| \leq N/2$. Because of the dealiasing pseudospectral numerical method, the simulation has $|k_i| \leq N_i/2 \cdot 2/3 = N_i/3$. That means even for $N_i = 1024$, $k_i \leq 341$ (including the dissipation range), which is significantly shorter than the inertial range of the solar wind spectrum (which has 2 to 3 decades).

One important difference between a randomly phased AW/KAW field and turbulence is the coherent structures, which have sharp boundaries and in which the fluctuation amplitude is larger than the rms fluctuation amplitude. These structures efficiently change the particle magnetic moments. In this paper, we study the relation between the resolution of the turbulence simulation and the heating rate.

In the simulations, the particles start out with a Maxwell distribution of velocities with temperature T. The initial test-particle mean gyroradius is defined as

$$\rho = \frac{v_\perp}{\Omega}, \tag{4.14}$$

where $v_\perp = \sqrt{2k_B T/m}$ and $\Omega = qB/mc$. We define

$$k_\rho = \frac{1}{\rho}. \tag{4.15}$$

By varying T, ρ amd m, any desired combination of the three quantities ϵ, $\beta = 8\pi n k_B T/B_0^2$ and k_ρ can be obtained.

The total-energy spectrum has a $k^{-1.5}$ spectral slope in the inertial range, as shown in Figure (4-3). The magnetic spectrum is steeper than the velocity spectrum. In this work, we focus on the velocity spectrum because it is δu that appears in Equation (3.16). The velocity spectrum is flatter and will be compensated by $k^{1.33}$ in the plots in the following sections.

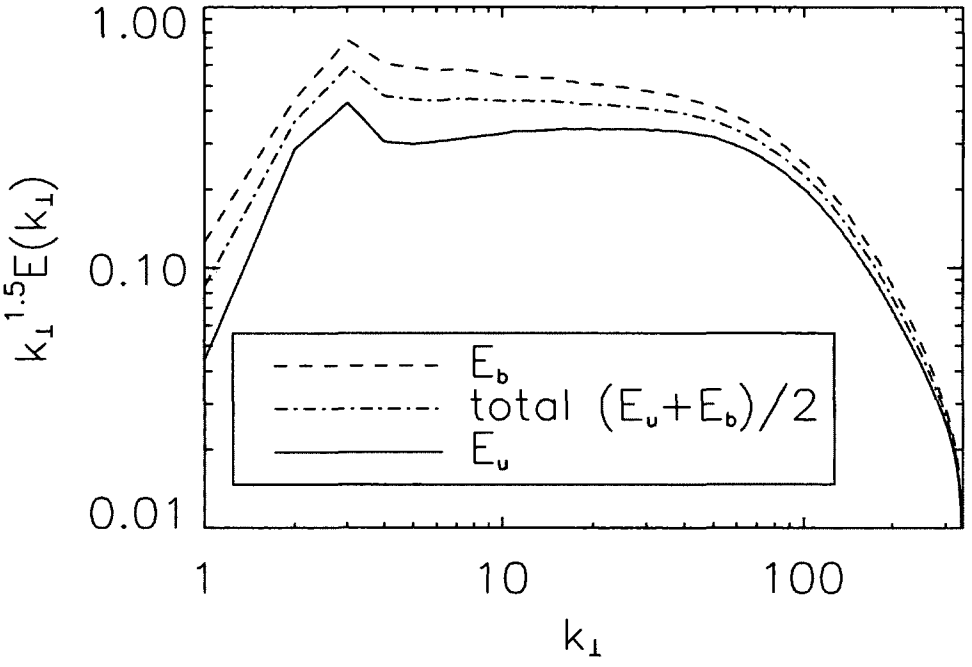

Figure 4-3. Power spectra in RMHD turbulence

The dash-dot line is $k^{1.5}(u(k)^2 + b(k)^2)/2$, the solid line stands for $k^{1.5}u(k)^2$, and the dashed line shows $k^{1.5}b(k)^2$.

The viscosity controls the breadth of the inertial range, which is limited by the numerical resolution. Too small viscosity causes instabilities that cause the code

to crash. With limited computational power, the spectrum cannot be extended as far as desired. For example, 1024^3 RMHD simulation for 150 eddy turnover times takes $\sim$ 7 million hours on 2048 CPUs. In some of our simulations, the dissipation term $-\nu\nabla^2\mathbf{z}^{\pm}$ ($p = 1$) in Equation (4.1) is replaced with a hyperviscous term of the form $-(\nu\nabla^2)^3\mathbf{z}^{\pm}$ ($p = 3$), or $-(\nu\nabla^2)^4\mathbf{z}^{\pm}$ ($p = 4$). Hyperviscosity can extend the spectrum's inertial range to higher k with the same resolution. When hyperviscosity is used, the break point between the inertial range and dissipation range is more dramatic. We define the dissipation wavenumber

$$k_d^2 = \frac{\int k_\perp^4 E_u(k_\perp)}{\int k_\perp^2 E_u(k_\perp)}. \tag{4.16}$$

The velocity spectra and associated values of k_d for several different runs are shown in Figure (4-4).

4.4 The Modification of the Velocity Distribution

In all of our simulations, we initialize the particles with Maxwellian distribution functions. In these simulations we have not addressed the effect of the stochastic heating on the particle distribution function.

However, in Figure (4-6) we present results from a simulation in which all particles start off with the same energy. The distribution function $f(v,t)$ is defined from

$$f(v,t) = \frac{1}{N}F(v,t), \tag{4.17}$$

and

$$N = \int_{-\infty}^{\infty} F(v,t)dv, \tag{4.18}$$

where N is the total number of all the test particles.

At the beginning of the simulation shown in Figure (4-6), the distribution is a δ function, which means all the particles have the same speed. This is flattened at

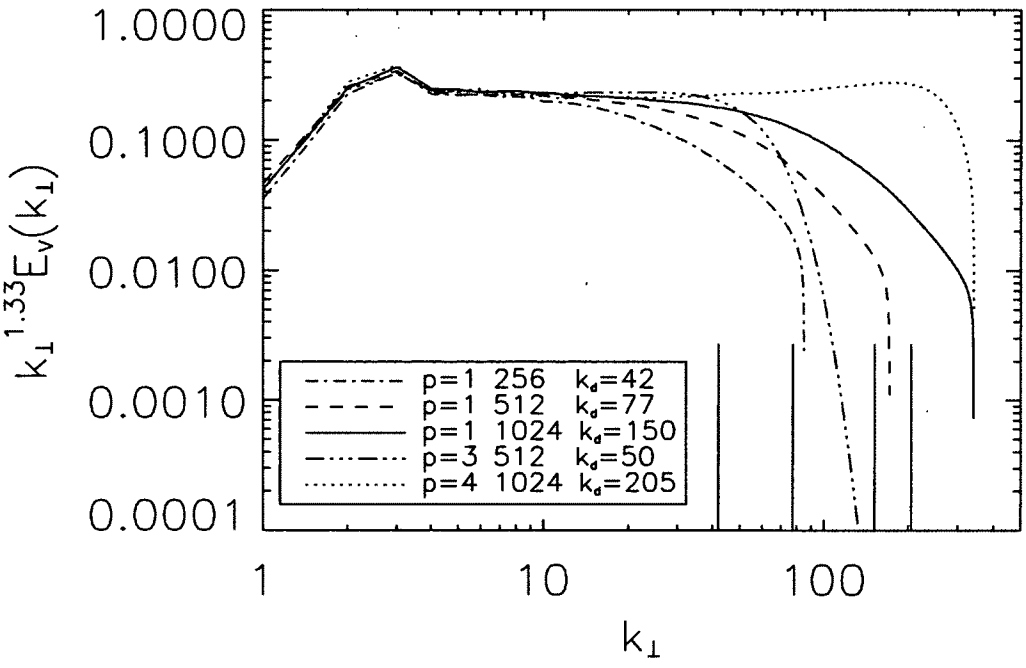

Figure 4-4. Spectra in different simulations with ordinary viscosity ($p = 1$) or hyperviscosity ($p = 3$ or $p = 4$)

These are the velocity spectra in simulations with different resolutions, 256^3 (referred as 256), $512^2 \times 256$ (512) and $1024^2 \times 256$ (1024) with normal viscosity or hyper viscosity ($p = 1, 3, 4$).

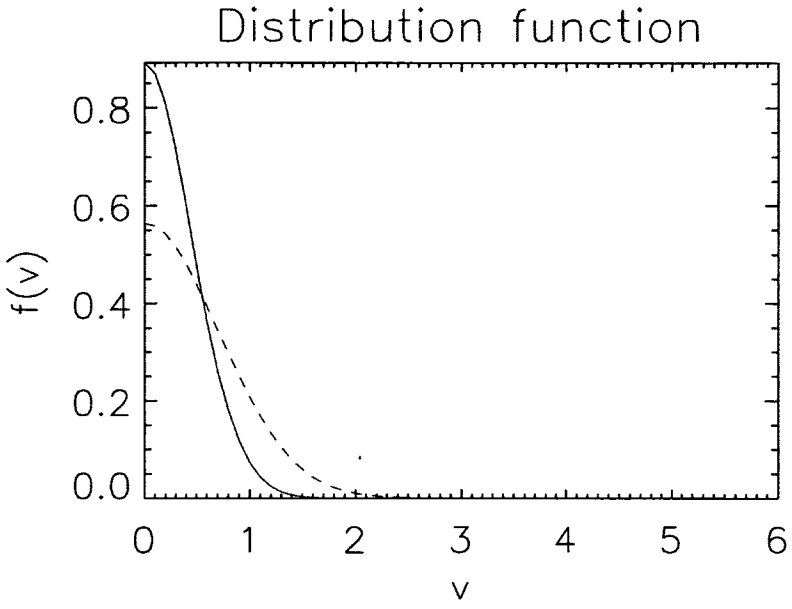

Figure 4-5. The time evolution of the distribution function

The normalized distribution function vs. velocity. The solid line is at $t = 0$; the dashed line comes from a later time.

a later time. Because the distribution function can not extend to negative speeds, the particles begin to be reflected back by the " $v = 0$ wall", and accumulate at low velocity. The distribution becomes small when it goes to higher velocity. It features that more particles are located at low velocity part, even the part near $v = 0$ is still sunken because of our limited simulation time. This proves that stochastic process, which beaks the magnetic moment conservation, accelerates/decelerates the particles randomly and flatten the distribution function in the velocity space.

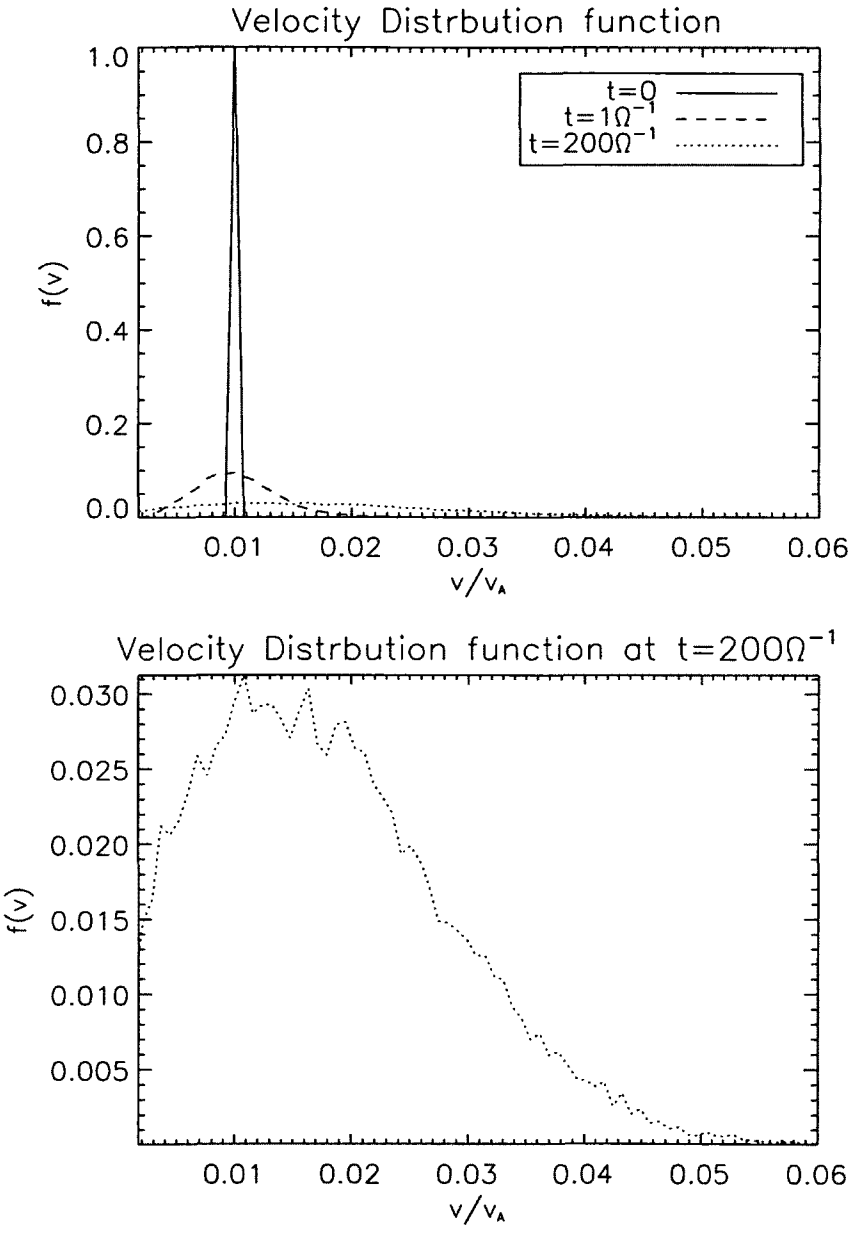

Figure 4-6. The velocity distribution function

The normalized distribution function $f(v,t)$ vs particle velocity. The data come from $t = 0, 1\Omega^{-1}, 200\Omega^{-1}$. The bottom panel is the zoomed picture of $t = 200\Omega^{-1}$. Here Ω is the test-particle gyrofrequency. The simulation traces particle trajectories in a superposition of randomly phased AWs and KAWs.

4.4.1 The Result of c_2 for the Same k_ρ

In our simulations, the wavenumber $k = 10$ is generally in the inertial range. We have carried out several numerical simulations using the RMHD code and choosing $k_\rho = 10$. The main results are listed in Table (4.1) and plotted in Figure (4-8). The examples of the $Q_\perp$ vs ϵ results for fitting the parameters c_1 and c_2 in Equation (3.16) are in Figure (4-7), where the simulations with normal viscosity are presented. For a fixed viscosity type ($p = 1$, 3, or 4), c_2 is decreasing as the perpendicular resolution increases and the viscosity decreases. This is due to the increased breadth of the inertial range, or some other mechanisms in turbulence, not the resolution itself. In Appendix A.5.4, the test-particle code is tested for the same Re, where $Re = uL/\eta$ is the Reynolds number at the outer scale L (i.e. the same width of inertial range) in simulations with different resolutions, and the values of c_2 are virtually the same.

When the resolution is fixed, 256^3 for example, c_2 is decreasing as p increases and k_d becomes larger. This suggests that the extension of the inertial range increases the heating rate. The bottom limit of c_2 in Run E1, E2, and E3 of Table 4.1 will be discussed in Section 4.4.3.

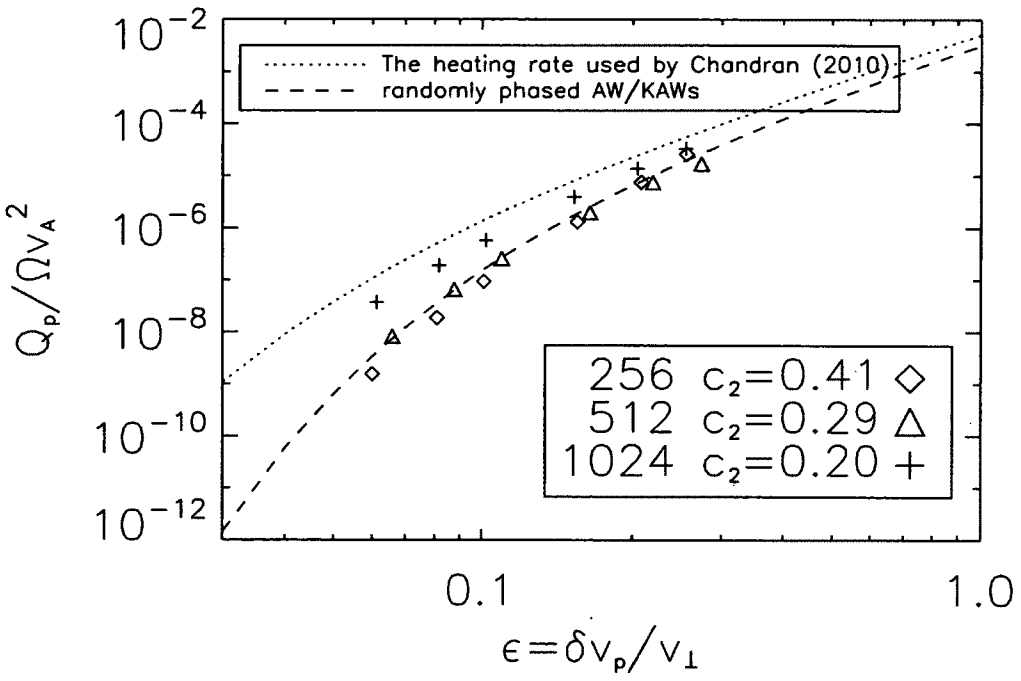

Figure 4-7. $Q_\perp$ vs ϵ, $k_\rho = 10$

The symbols represent data in A2, A3, and A4 of Table 4.1. $\epsilon = 0.06 \sim 0.25$ and $p = 1$. The dashed line uses $c_2 = 0.15$ as *Chandran et al.* (2010) used to match the ion temperature in the coronal holes.

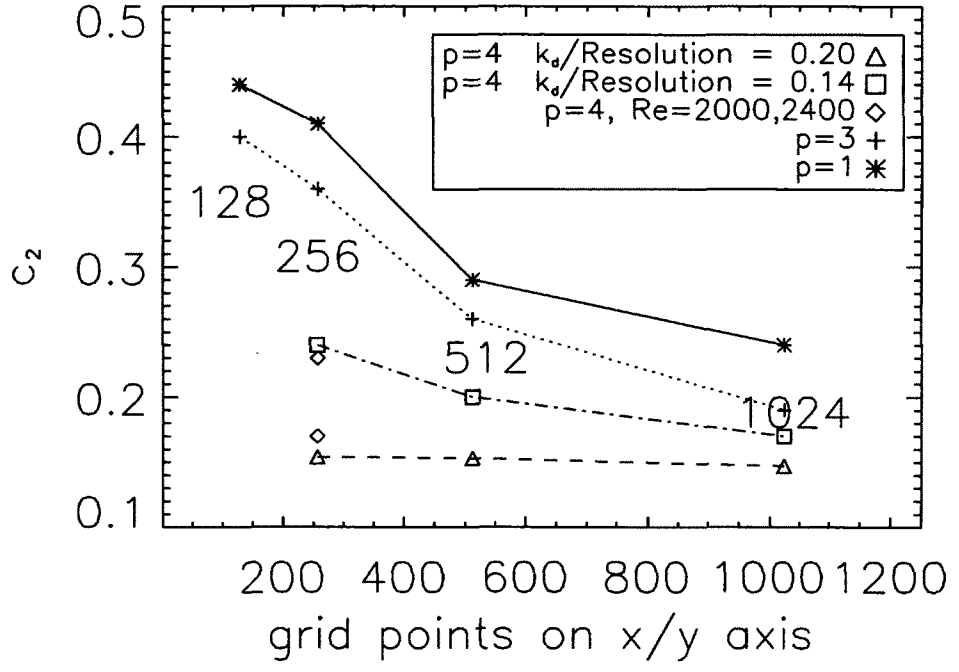

Figure 4-8. c_2 vs resolution, $k_\rho = 10$

The symbols on the same line come from the simulations which have the same order of hyperviscosity($p = 1, 3, 4$). For each symbol type, k_d is proportional to the resolution.

Table 4.1. Summary of simulations with $k_\rho = 10$

Runs	p	Resolutions	Re	k_d	c_2
A1	1	128^3	384	29	0.44
A2	1	256^3	960	42	0.41
A3	1	$512^2 \times 256$	2400	77	0.29
A4	1	$1024^2 \times 256$	6000	150	0.20
B1	3	128^3	384	18	0.41
B2	3	256^3	960	27	0.36
B3	3	$512^2 \times 256$	2400	49	0.26
B4	3	$1024^2 \times 256$	10141	96	0.18
C1	4	256^3	1800	36	0.24
C2	4	$512^2 \times 256$	6778	72	0.20
C3	4	$1024^2 \times 256$	16421	144	0.17
D1	4	256^3	2000	38	0.23
D2	4	256^3	2400	41	0.17
E1	4	256^3	3400	52	0.15
E2	4	$512^2 \times 256$	12736	103	0.15
E3	4	$1024^2 \times 256$	35840	206	0.15

4.4.2 The Result of c_2 for Different k_ρ

In the first part of this section, we consider sets of simulations in which k_ρ varies with the resolution so as to keep the ratio k_ρ/k_d fixed in Table 4.2 and Figure (4-10). The $Q_\perp$ vs ϵ results of normal viscosity ($p = 1$) are in Figure (4-9). This means that there is the same amount of "spectrum" at $k > k_\rho$ in each simulation within a set (e.g. in runs F1, F2, and F3). The quantity $k_d \Delta x$ is also roughly constant in each set of simulations, where Δx is the grid spacing in the xy-plane. This means that there is the same number of grid points across a gyro-orbit in each simulation.

For the runs with ordinary viscosity, $p = 1$ (the solid line in Figure 4-10), increasing the resolution and k_ρ simultaneously leads to a significant increase in the heating rate (i.e. decrease in c_2). As we discuss further below, we conjecture that this is because of the increased intermittency (kurtosis, see Section 4.4.3) at $k = k_\rho$ in the higher-resolution runs. We defer our discussion of the hyperviscous runs until Section 4.4.3.

The lack of convergence is related to the lack of the measurement of the turbulence intensity.

Table 4.2. Summary of simulations at different k_ρ

Runs	p	Resolutions	Re	k_ρ	k_ρ/k_d	results (c_2)
F1	1	256^3	960	10	0.24	0.41
F2	1	$512^2 \times 256$	2400	20	0.26	0.40
F3	1	$1024^2 \times 256$	6000	40	0.27	0.26
G1	3	256^3	960	10	0.37	0.36
G2	3	$512^2 \times 256$	2400	20	0.40	0.37
G3	3	$1024^2 \times 256$	10141	40	0.42	0.31
H1	4	256^3	1800	10	0.28	0.24
H2	4	$512^2 \times 256$	2400	20	0.28	0.29
H3	4	$1024^2 \times 256$	16421	40	0.28	0.29
I1	4	256^3	3400	10	0.19	0.15
I2	4	$512^2 \times 256$	12736	20	0.19	0.16
I3	4	$1024^2 \times 256$	35840	40	0.19	0.16

In the second part of this section, we vary k_ρ within a single RMHD simulation by introducing several cohorts of test particles and tracking their evolution simultaneously. We carry out this procedure for two RMHD simulations, J1-J4 and K1-K5 (see Figure 4-11), with properties summarized in Table 4.3 and Figure (4-12).

Table 4.3. $1024^2 \times 256$ simulations for different k_ρ

Runs	p	Re	k_ρ	results (c_2)	c_1
J1	4	35840	10	0.15 ± 0.02	0.82
J2	4	35840	20	0.15 ± 0.03	0.76
J3	4	35840	40	0.16 ± 0.03	0.73
J4	4	35840	80	0.19 ± 0.04	0.69
K1	1	6000	10	0.20 ± 0.04	0.71
K2	1	6000	20	0.22 ± 0.02	0.68
K3	1	6000	40	0.26 ± 0.03	0.63
K4	1	6000	80	0.21 ± 0.04	0.74
K5	1	6000	160	0.15 ± 0.03	0.94

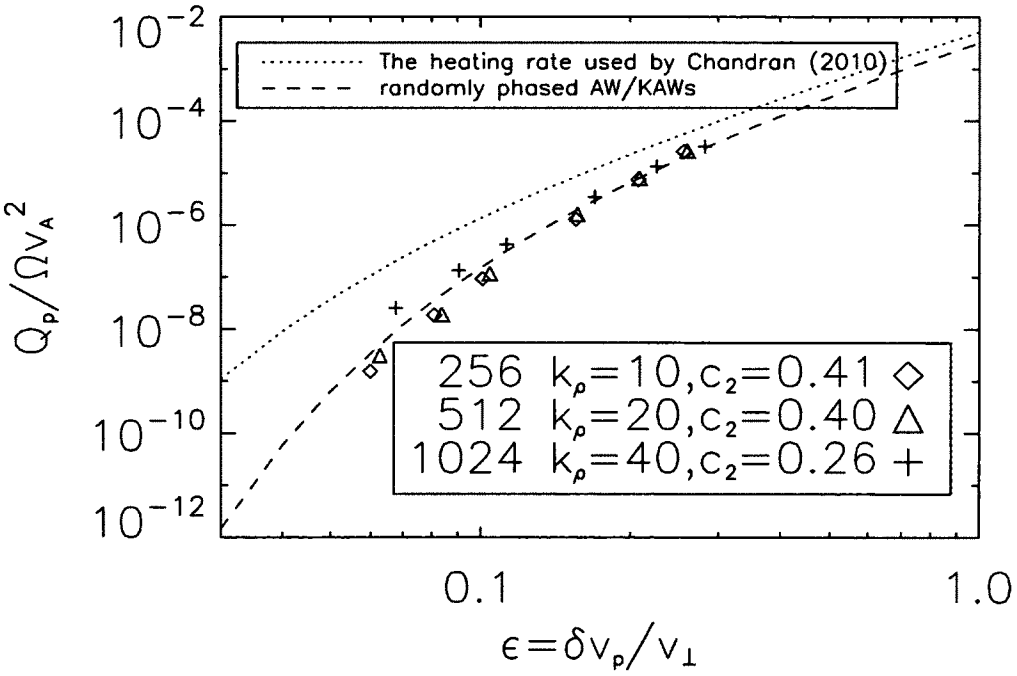

Figure 4-9. $Q_\perp$ vs ϵ for different k_ρ

The symbols represent data in F1, F2, and F3 of Table 4.2. $\epsilon = 0.06 \sim 0.25$ and $p = 1$.

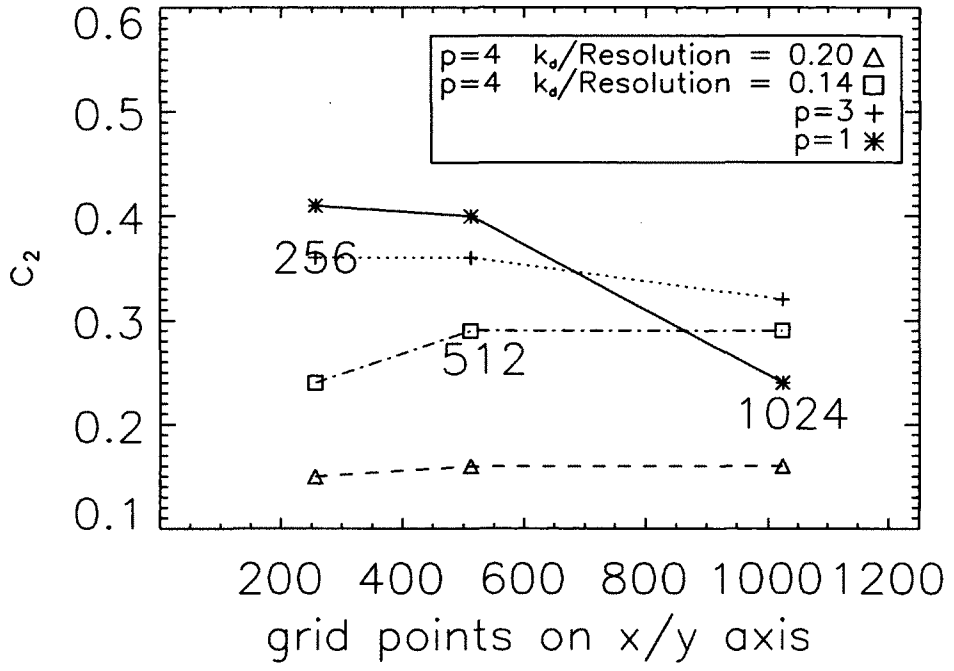

Figure 4-10. c_2 vs resolution for different k_ρ

The symbols on the same line come from the simulations which have the same order of hyperviscosity($p = 1, 3, 4$). The set up of k_d is same as Figure (4-8). The difference is that k_ρ also doubles with the perpendicular resolution in Table 4.2.

For the $p = 1$ runs (K1 - K5), there are two trends apparent from Table 4.3. First, as k_ρ increases from 10 to 40, there is a slight increase in c_2 (reduction in $Q_\perp$). We conjecture that this may be due to a modest contribution to the heating rate and μ-nonconservation from the large-scale forcing, as was found previously by *Lehe et al.* (2009), although in their case the effects of the large-scale forcing were larger since the force was randomized at each time step, leading to high-frequency fluctuations. Second, as k_ρ increases from 40 to 160, there is a significant reduction in c_2. We conjecture that this may be due in part to the increase in the intermittency at $k = k_\rho$ as k_ρ increases (see next section). It may also be due in part to a contribution to $Q_\perp$ from fluctuations with $k \ll k_\rho$. This is a possibility because c_2 is calculated from Equation (3.16) based on the value of δu_ρ. As k_ρ increases into the dissipation range, δu_ρ becomes increasingly small, and so a modest contribution to $Q_\perp$ from fluctuations with $k \ll k_\rho$ could lead to a significant decrease in c_2.

For the $p = 4$ runs, the variation of c_2 with k_ρ is different. We also defer our discussion of these runs until Section 4.4.3.

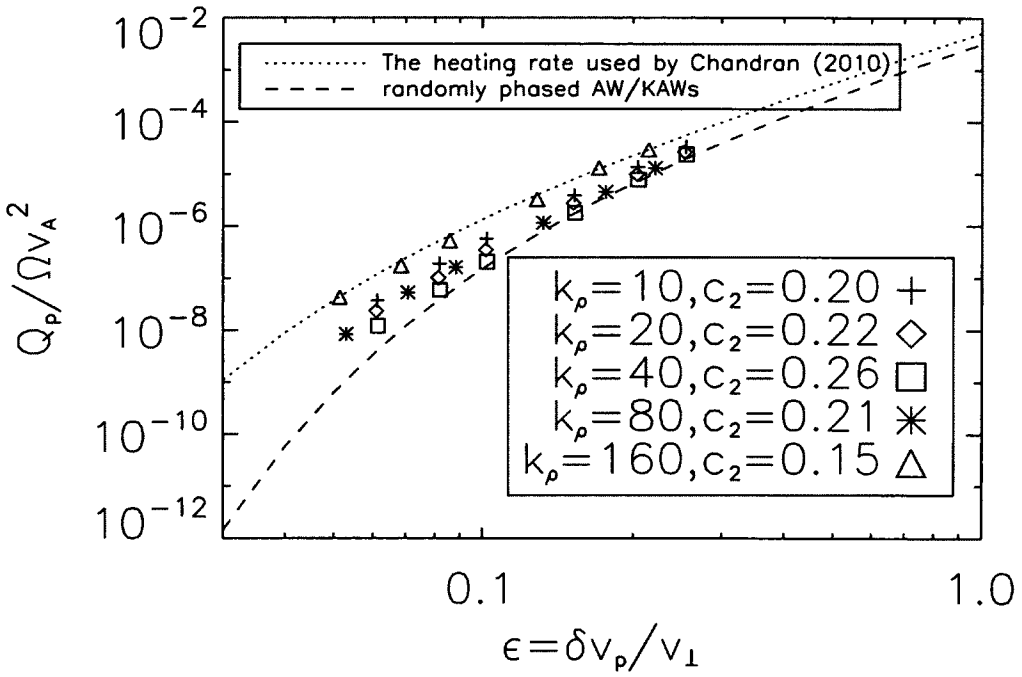

Figure 4-11. $Q_\perp$ vs ϵ in the same simulation

The symbols represent data in K1 - K5 of Table 4.3. $\epsilon = 0.05 \sim 0.25$ and $p = 1$.

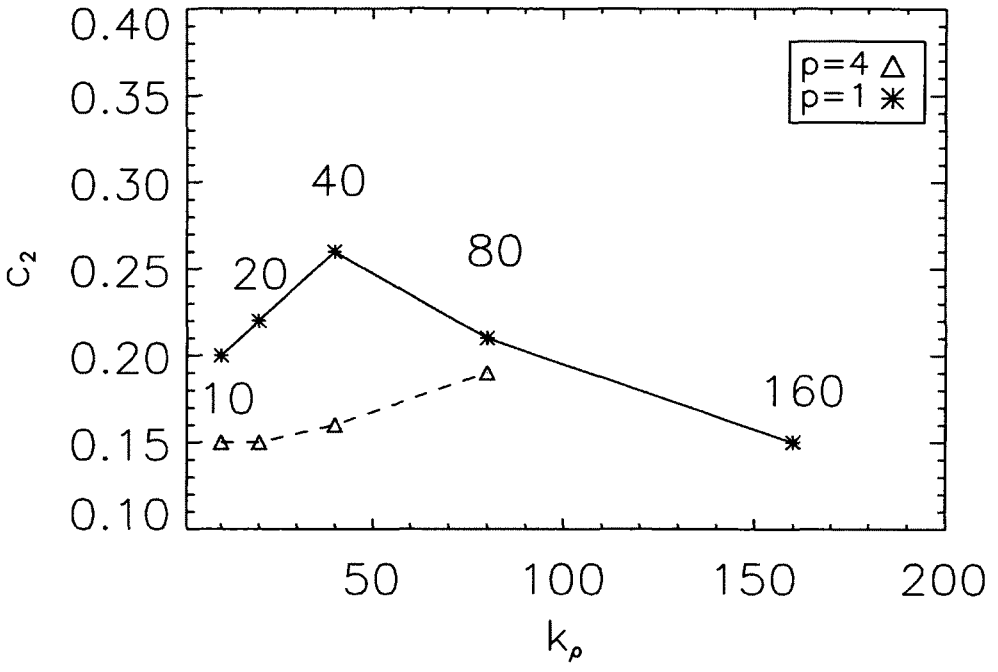

Figure 4-12. c_2 vs k_ρ in the same simulation

The symbols on the same line come from the same $1024^2 \times 256$ simulation. $p = 1$, or 4.

4.4.3 Intermittency in the RMHD Simulations

In numerical simulations of turbulence, hyperviscosity not only can stabilize the code, but also may make the result unphysical, leading to effects such as the bump in the spectrum near k_d in the $p = 4$ simulation with $1024^2 \times 256$ grid points (see Figure 4-3). This bottleneck has been earlier studied by *Frisch et al.* (2008). Although hypervisocity can be used to extend the spectrum, too high a value of p could destroy coherent structures and reduce intermittency at all scales.

The kurtosis can be used to measure the degree of intermittency and the presence of coherent structures. In statistics, it is calculated from a n-element ensemble, $(x_0, x_1, ..., x_{n-1})$, as

$$Kurtosis = \frac{1}{n}\sum_{j=0}^{n-1}\left(\frac{x_j - \bar{x}}{\sqrt{Variance}}\right)^4 - 3, \tag{4.19}$$

where

$$Variance = \frac{1}{n-1}\sum_{i=0}^{n-1}(x_i - \bar{x})^2. \tag{4.20}$$

In Figure (4-13), the averaged kurtosis of $\mathbf{z}^{\pm}$ in Equation (4.1) at different scales in different simulations is calculated. A randomly-phased AW/KAW field obeys Gaussian statistics and has a kurtosis of 0. The kurtosis departs from zero and becomes larger as more intermittency is present in the turbulence field. The bottom three lines in Figure (4-13) come from the $p = 4$ simulation with bumps in the spectrum near the dissipation wavenumber k_d, which also lead to the smallest values of c_2 in Figure (4-8). Normal viscosity ($p = 1$) and hyper viscosity ($p = 4$) here show different behaviors. As $k_\perp$ increases in the $p = 1$ simulation; the kurtosis increases to an average > 6. In the $p = 4$ simulations the kurtosis stops growing at $k \sim 20 - 40$, reaching a maximum value of ~ 2.5. This shows that normal viscosity leads to the development of more coherent structures than hyperviscosity. However, $p = 1$ does

not produce a higher heating rate than $p = 4$. We suspect that the very high heating rates ($c_2 \sim 0.15$) seen in our $p = 4$ runs result from unphysical fluctuations at small scales. As *Frisch et al.* (2008) have argued, the spectral "bumps" at high-k in runs with hyperviscosity are an unphysical numerical artifact that can lead to spurious results, such as the destruction of coherent structures, or the isotropization of fluctuations. For these reasons, we believe that our $p = 1$ runs are more relevant to turbulence and stochastic heating in the corona and solar wind than are our runs with hyperviscosity.

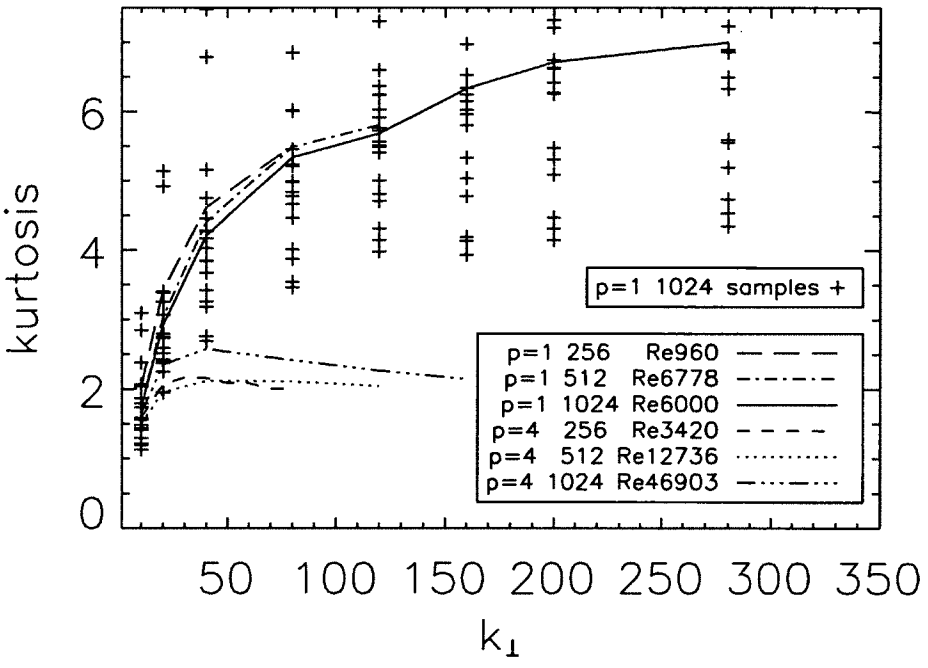

Figure 4-13. Kurtosis at different scales

The effect of hyperviscosity on kurtosis at different scales. + are the data for $1024^2 \times 256$ simulations with $p = 1$. The solid line is the average of those data at different $k_\perp$.

4.4.4 The Effect of the Spectral Slope

In this section, the average spectral index n (such as $E(k_\perp) \propto k_\perp^{-n}$) is calculated near k_ρ, averaging over the wavenumber range, $(e^{-0.5}k_\rho, e^{0.5}k_\rho)$. Simulations with $p = 1$ and $p = 4$ again differ as shown in Figure (4-14).

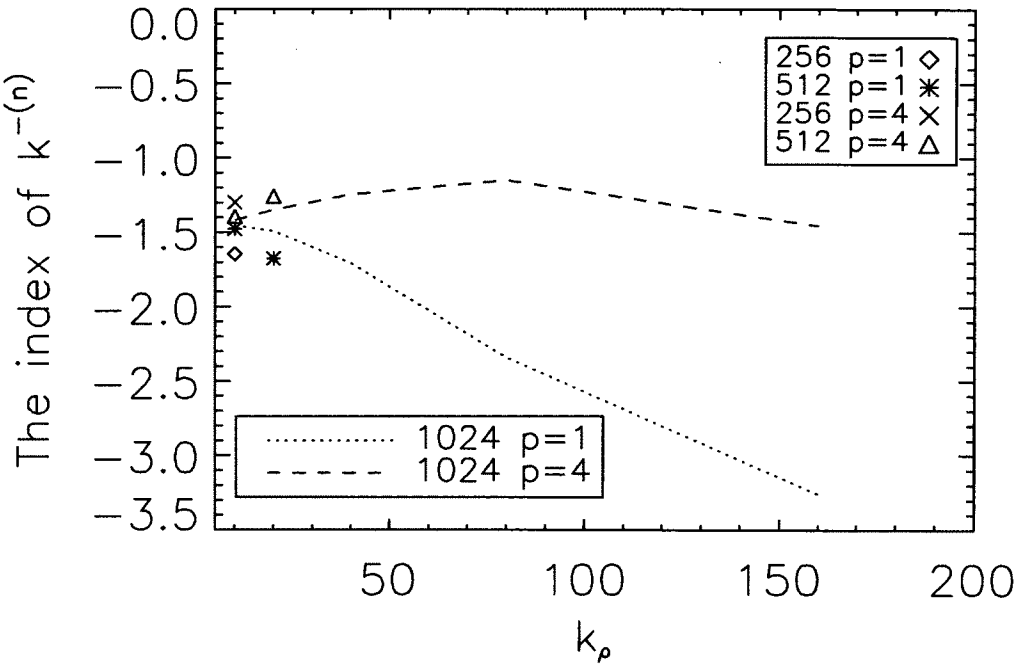

Figure 4-14. The spectral slope near k_ρ

Here a power spectrum k^{-n} is assumed. The average domain is not on k_ρ exactly, but on a longer range $(e^{-0.5}k_\rho, e^{0.5}k_\rho)$.

Simulations with $p = 1$ have steeper spectral slopes at larger $k_\perp$. In contrast, the spectrum in the $1024^2 \times 256$ simulation with $p = 4$ becomes flatter as k increases from 0 to 80. The dependence of c_2 on the spectral index n is explored in Figure (4-15). For runs with ordinary viscosity, the heating rate is smaller (i.e. c_2 is larger) when the spectrum is steeper in the inertial range ($k_\rho = 10, 20, 40$ case). $k_\rho = 80, 160$ with

$p = 1$ has been discussed in Section 4.4.2. In the runs with $p = 4$, c_2 is less sensitive to the value of n.

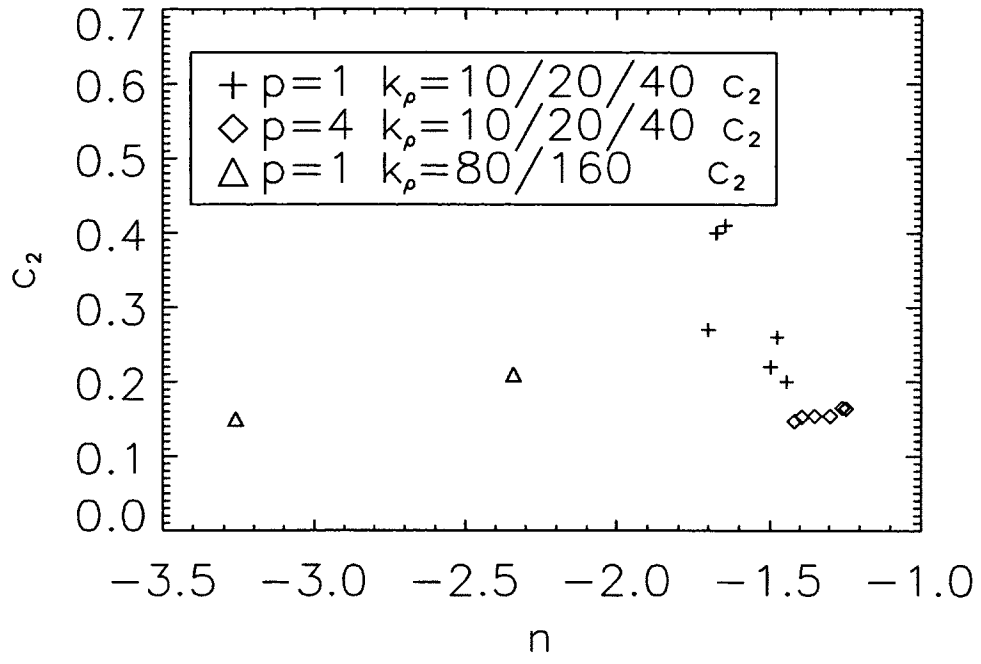

Figure 4-15. c_2 vs the slope index near k_ρ

4.4.5 The Effect of β and Parallel Heating

When β is as small as 0.006 in the most parts, it is safe to ignore Landau damping for small ϵ. On another side, stochastic heating does not explicitly explain the role of β in the heating rate. In this part, different β is tested in 256^3, and $512^2 \times 256$ resolutions with normal viscosity in Figure (4-16). The Re is the same as A2, A3 in Table 4.1. The result shows that the change of β does not affect the heating rate much when β is below 1.0.

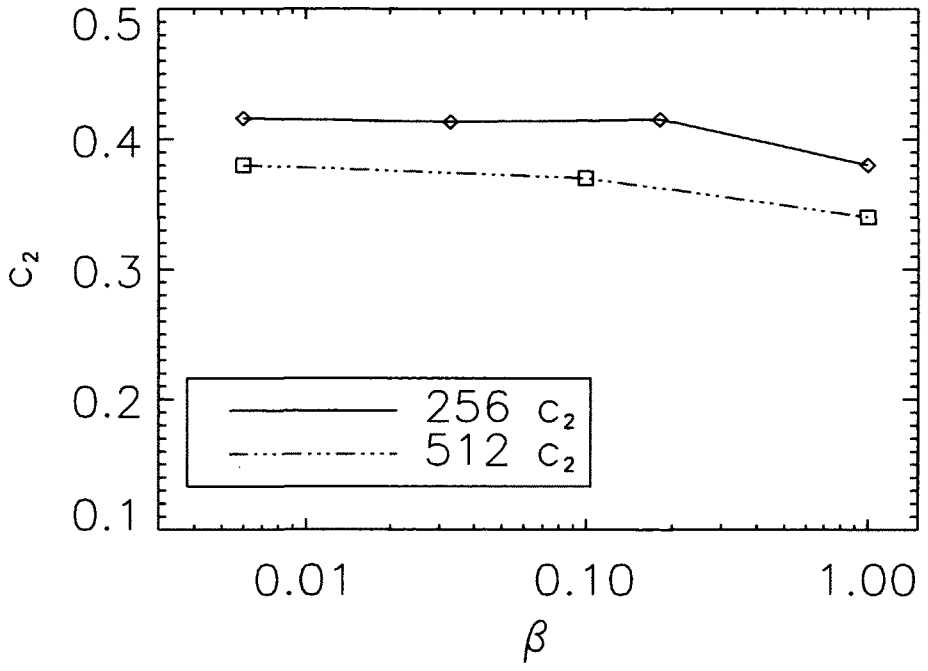

Figure 4-16. c_2 vs β

β is chosen to be 0.006, 0.033, 0.1, 0.18, 1.0 in different simulations.

As mentioned in Chapter ??, $v_T \ll V_A$ is found in the low-β solar wind close to the Sun. The Landau damping condition $\omega_A - k_\parallel v_\parallel = 0$ is not satisfied. In the RMHD simulations, δE_z and δB_z are also zero, which eliminates linear Landau damping and linear transit-time damping. Although stochastic heating can increase $T_\parallel$, *Chandran et al.* (2010) showed that the parallel heating rate $Q_\parallel$ is $\ll Q_\perp$ by setting

$$Q_\parallel = \frac{1}{2}\left(\frac{< v_{\parallel f}^2 > - < v_{\parallel 0}^2 >}{t_f - t_0}\right) \tag{4.21}$$

where the notation is the same as in Equation (4.11). Figure (4-17) shows the ratio of the parallel heating rate to the perpendicular one for different ϵ. $Q_\parallel/Q_\perp$ is generally ≤ 0.01.

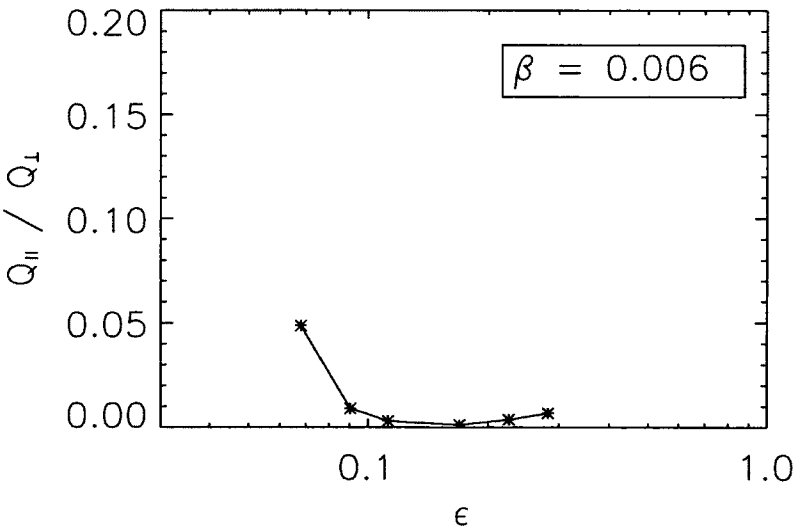

Figure 4-17. Parallel heating vs perpendicular heating

The data comes from the $512^2 \times 256$ resolution simulation with normal viscosity, and $\beta = 0.006$.

When β approaches 1, Landau damping begins to be important. The similar simulation as A2 in Table 4.1 re-runs with $\beta = 1$ (The setup of RMHD simulations is

not changed). The result for $k_\rho = 10$ is in Figure (4-18). Both heating rates $Q_\perp$ and $Q_\parallel$ are high. Now comparing to $Q_\perp$, $Q_\parallel$ is much higher ($Q_\parallel/Q_\perp < 0.05$ when $\beta = 0.006$ in Chapter 4.4.5). Even the $E_\parallel$ derived in RMHD is underestimated (*Lehe et al.*, 2009). But $Q_\parallel$ is still larger than $Q_\perp$ for small ϵ with this underestimated parallel electric field. While for large ϵ, $Q_\parallel$ approaches $Q_\perp$ as the simulation evolves. The temperature comes back to quasi-isotropic in the limited running time ($< V_\perp^2 > / < V_\parallel^2 > \Rightarrow 2$), as in Figure (4-19).

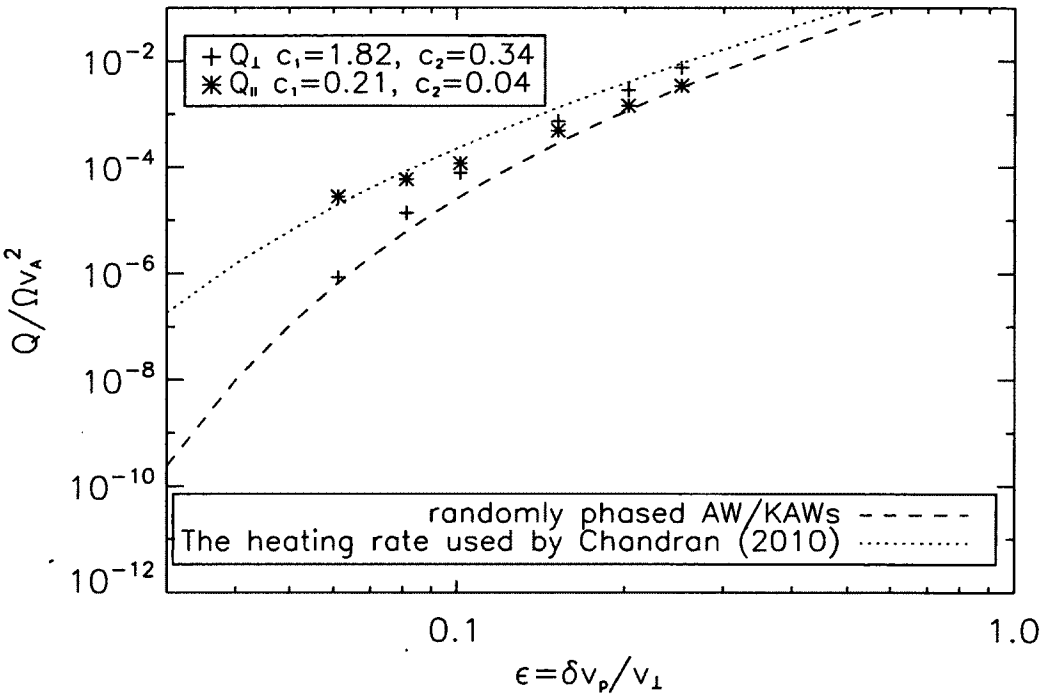

Figure 4-18. $Q_\perp$ and $Q_\parallel$ vs ϵ for $\beta = 1$

The 256^3 RMHD simulation with $p = 1$ has the same parameters as A3 in Table 4.1. $k_\rho = 10$ is also applied here.

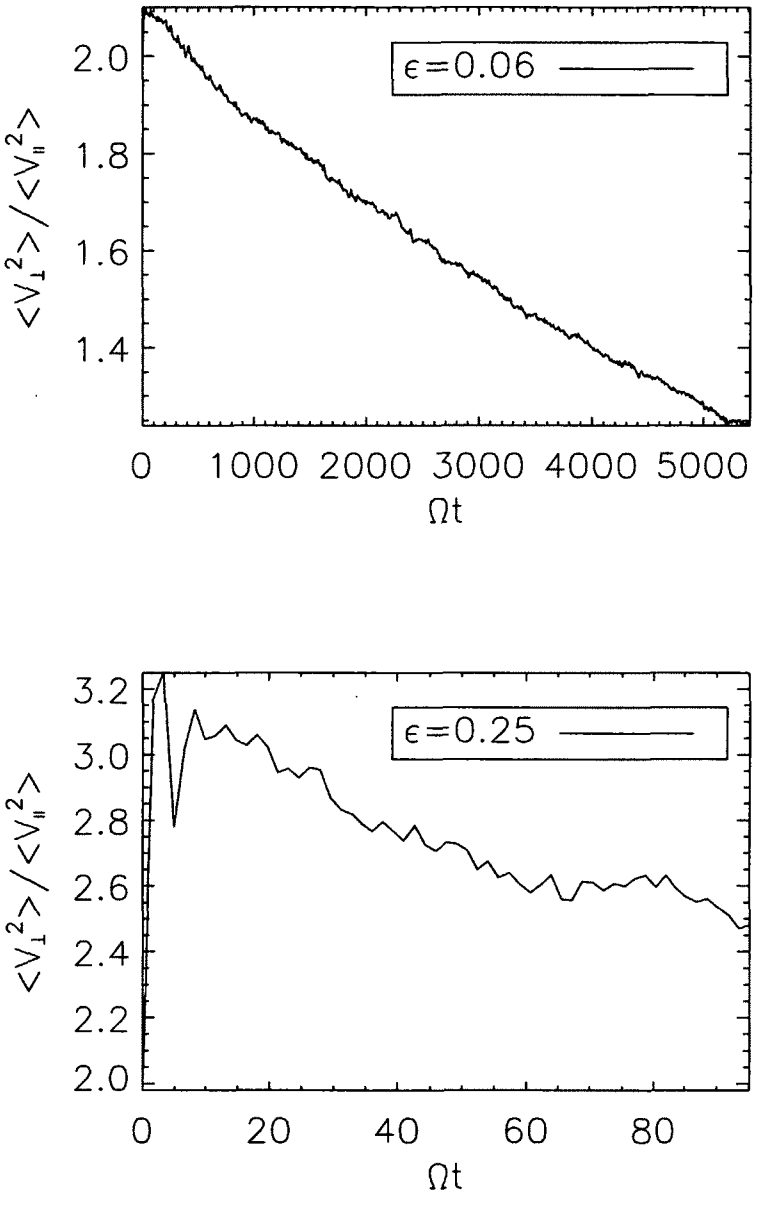

Figure 4-19. $T_\perp/T_\parallel$ vs time for different ϵ with $\beta = 1$

The ratio of the perpendicular temperature to the parallel temperature vs time for $\epsilon = 0.06, 0.25$ in Figure (4-18).

CHAPTER 5

CONCLUSION

The stochastic heating is seen in new test particle simulations based on a RMHD code. It can flatten the distribution of test particles as a diffusion process. The heating rate $Q_\perp$ is found to be larger than in the case of particles interacting with randomly-phased Alfvén waves and kinetic Alfvén waves. This agrees with the idea that coherent structures in turbulence, in which the fluctuating fields are larger than their rms values, enhance the stochastic heating rate.

In these simulations with low-β ($\beta = 0.006$), the relation among the Re, gyroradius k_ρ^{-1} of test particles, the simulation resolution, and normal viscosity & hyper viscosity is studied. When k_ρ is in the inertial range, the broadening of the inertial range can increase the perpendicular heating rate $Q_\perp$, and a flatter spectral slope can generate more heating. When k_ρ goes deep in the inertial range, c_2 increases, which could be a result of disappearing of the effect of the large-scale force on the particles. When it even reaches the dissipation scales, c_2 decreases, which may agree with the enhancement of intermittency in the small scales, or a result of more fluctuations at larger scales. It suggests the wave-particle interaction scales of the stochastic heating may be broader than the one we used for δu in Equation (3.16).

On the other side, the turbulence fields from RMHD simulations can produce more heating, and parallel heating becomes more important when β approaches 1, even though it does not include the magnetosonic waves (*Lehe et al.*, 2009).

When we use hyperviscosity to study turbulence which is a good way to extend the inertial range for a given resolution, the test-particle simulation suggests that it

not only changes the dissipation scales and may cause an unphysical bottleneck near k_d, but also affects the whole spectrum in a way that can heat the test particles much stronger. In this upper limit, the breadth of the inertial range does not change the heating rate as much as it does in the normal viscosity case.

In our limited-resolution simulations with normal viscosity ($p = 1$), the maximum $k_d = 150$ with a $1024^2 \times 256$ resolution. While the outer scale has $1 \leq k_o \leq 2$, which means $k_d/k_o < 100$. This value is much larger in the solar wind (*Dmitruk et al.*, 2002). Many c_2 are obtained in the above simulations depending on the initial numerical turbulence condition. $k_\rho = 80$ in $1024^2 \times 256$ simulation with normal viscosity (see Figure 5-1) would give the most probable parameter, $c_2 = 0.21 \pm 0.04$, for thermal protons in the solar wind. Because it is suggested that the break point k_b between the inertial range and dissipation scales has $k_b\rho \sim 1$ in the solar wind, where ρ is the gyroradius of thermal protons (*Bale et al.*, 2005). Even the dissipation scales are believed to dissipate more fluid and magnetic energy, $k_\rho = 160$ may not be a good optional case here. Because the dissipation range in RMHD numerical simulation does not have much physical meaning and does not show the electric field spectrum is flatter than the corresponding magnetic spectrum as reported in Hall MHD study (*Matthaeus et al.*, 2010). We also need to notice that the grid length $\Delta x = 2\pi/1024$ for the 1024^2 resolution on the perpendicular plane, which means one gyroradius of $k_\rho = 80(160)$ only includes 2(1) grid point. Because the interpolation of the field on grid points smoothes out the details, it is reasonable to believe that c_2 would be modestly smaller than what we obtained here.

So far, the heating rate from test-particle simulations is not larger than the one used by *Chandran et al.* (2010), which can fit the temperature of different ions near $2R_s$ based on observation constrains. However, it is not sure if this is the upper limit of stochastic heating. This is crucial for the solar-wind heating problem. The missing of

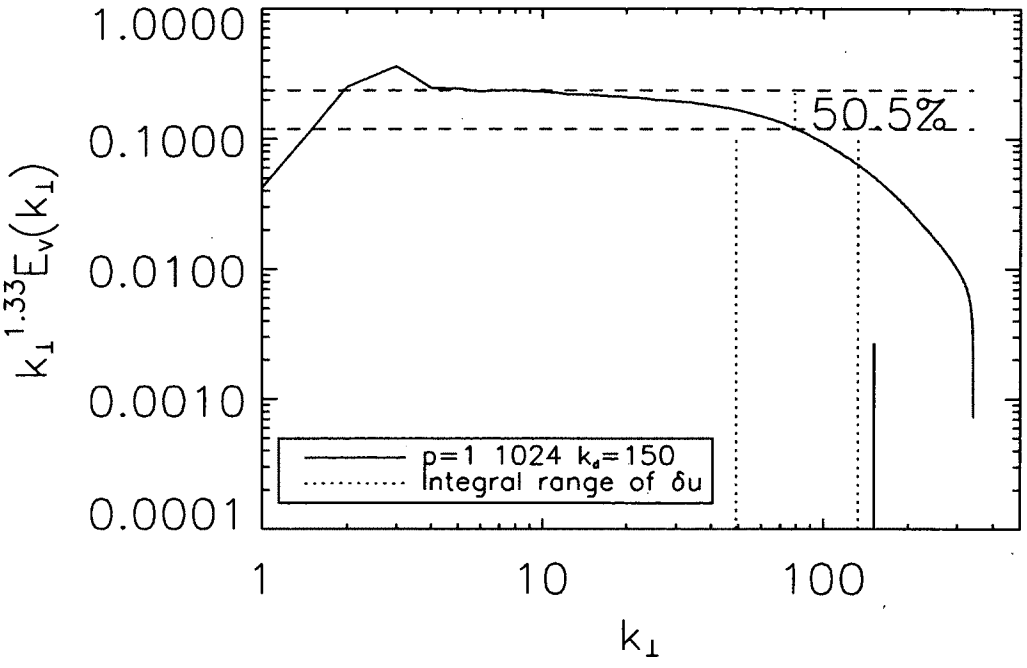

Figure 5-1. The spectrum of the $1024^2 \times 256$ simulation with ordinary viscosity ($p = 1$)

The top dash line is the extension of the inertial range with a spectral slope of $k^{-1.33}$. The actual fluctuating velocity power at $k = 80$ is just 50.5% of what is expect for a longer inertial range. The integral range of δu for $k_\rho = 80$ is $(49, 132)$.

high-frequency channels such as the cyclotron resonance from the observation makes this as a threshold between the powerful low-frequency Alfvén waves and mysteriously fast/hot solar wind. Although our results of the heating rate have not converged yet as shown in Figure (4-8) and (4-10), they suggest that the stochastic heating rate may indeed be large enough that low-frequency Alfvén wave turbulence could explain the observations of perpendicular ion heating. Further numerical simulations at larger resolution will be needed to place this conclusion on a firmer footing. Because the heating rate from these simulations are generated from Aflvén turbulence with limited energy spectra of short energy-spectrum inertial range and small intensity, which has been observed to affect the heating rate from the simulations here.

BIBLIOGRAPHY

Antonucci, E., M. A. Dodero, and S. Giordano (2000), Fast solar wind velocity in a polar coronal hole during solar minimum, , *197*, 115–134.

Bale, S. D., P. J. Kellogg, F. S. Mozer, T. S. Horbury, and H. Reme (2005), Measurement of the Electric Fluctuation Spectrum of Magnetohydrodynamic Turbulence, *Physical Review Letters*, *94*(21), 215,002–+, doi:10.1103/PhysRevLett.94.215002.

Bame, S. J., J. R. Asbridge, W. C. Feldman, and J. T. Gosling (1977), Evidence for a structure-free state at high solar wind speeds, , *82*, 1487–1492, doi:10.1029/JA082i010p01487.

Belcher, J. W., and L. Davis, Jr. (1971), Large-amplitude Alfvén waves in the interplanetary medium, 2., , *76*, 3534–3563.

Boris, J. (1970), in *Proceedings of the Fourth Conference on Numerical Simulation of Plasmas*, pp. 3–67, Naval Research Lab.

Chandran, B. D. G. (2005), Weak Compressible Magnetohydrodynamic Turbulence in the Solar Corona, *Physical Review Letters*, *95*(26), 265,004–+, doi:10.1103/PhysRevLett.95.265004.

Chandran, B. D. G. (2010), Alfvén-wave Turbulence and Perpendicular Ion Temperatures in Coronal Holes, , *720*, 548–554, doi:10.1088/0004-637X/720/1/548.

Chandran, B. D. G., and J. V. Hollweg (2009), Alfvén Wave Reflection and Turbulent Heating in the Solar Wind from 1 Solar Radius to 1 AU: An Analytical Treatment, , *707*, 1659–1667, doi:10.1088/0004-637X/707/2/1659.

Chandran, B. D. G., B. Li, B. N. Rogers, E. Quataert, and K. Germaschewski (2010), Perpendicular Ion Heating by Low-Frequency Alfven-Wave Turbulence in the Solar Wind, *ApJ, submitted*, (arXiv:1001.2069).

Chen, L., Z. Lin, and R. White (2001), On resonant heating below the cyclotron frequency, *Physics of Plasmas*, *8*, 4713–4716, doi:10.1063/1.1406939.

Cho, J., and A. Lazarian (2003), Compressible magnetohydrodynamic turbulence: Mode coupling, scaling relations, anisotropy, viscosity-damped regime and astrophysical implications, , *345*, 325–339, doi:10.1046/j.1365-8711.2003.06941.x.

Cranmer, S. R., and A. A. van Ballegooijen (2003), Alfvénic turbulence in the extended solar corona: Kinetic effects and proton heating, , *594*, 573–591, doi: 10.1086/376777.

Cranmer, S. R., and A. A. van Ballegooijen (2005), On the generation, propagation, and reflection of Alfvén waves from the solar photosphere to the distant heliosphere, , *156*, 265–293, doi:10.1086/426507.

Cranmer, S. R., A. A. van Ballegooijen, and R. J. Edgar (2007), Self-consistent Coronal Heating and Solar Wind Acceleration from Anisotropic Magnetohydrodynamic Turbulence, , *171*, 520–551, doi:10.1086/518001.

De Pontieu, B., et al. (2007), Chromospheric Alfvénic Waves Strong Enough to Power the Solar Wind, *Science*, *318*, 1574–7, doi:10.1126/science.1151747.

Dmitruk, P., W. H. Matthaeus, L. J. Milano, S. Oughton, G. P. Zank, and D. J. Mullan (2002), Coronal heating distribution due to low-frequency, wave-driven turbulence, , *575*, 571–577, doi:10.1086/341188.

Dmitruk, P., W. H. Matthaeus, and N. Seenu (2004), Test Particle Energization by Current Sheets and Nonuniform Fields in Magnetohydrodynamic Turbulence, , *617*, 667–679, doi:10.1086/425301.

Esser, R., S. Fineschi, D. Dobrzycka, S. R. Habbal, R. J. Edgar, J. C. Raymond, J. L. Kohl, and M. Guhathakurta (1999), Plasma properties in coronal holes derived from measurements of minor ion spectral lines and polarized white light intensity, , *510*, L63–L67, doi:10.1086/311786.

Feldman, W. C., S. R. Habbal, G. Hoogeveen, and Y. Wang (1997), Experimental constraints on pulsed and steady state models of the solar wind near the Sun, , *102*, 26,905–26,918, doi:10.1029/97JA02436.

Fisk, L. A. (2003), Acceleration of the solar wind as a result of the reconnection of open magnetic flux with coronal loops, *Journal of Geophysical Research*, *108*, 7, doi:10.1029/2002JA009284.

Frisch, U., S. Kurien, R. Pandit, W. Pauls, S. S. Ray, A. Wirth, and J.-Z. Zhu (2008), Hyperviscosity, Galerkin Truncation, and Bottlenecks in Turbulence, *Physical Review Letters*, *101*(14), 144501, doi:10.1103/PhysRevLett.101.144501.

Goldreich, P., and S. Sridhar (1995), Toward a theory of interstellar turbulence. 2: Strong alfvenic turbulence, , *438*, 763–775, doi:10.1086/175121.

Grappin, R., A. Mangeney, and E. Marsch (1990), On the origin of solar wind MHD turbulence - HELIOS data revisited, , *95*, 8197–8209, doi: 10.1029/JA095iA06p08197.

Hellinger, P., P. Trávníček, J. C. Kasper, and A. J. Lazarus (2006), Solar wind proton temperature anisotropy: Linear theory and WIND/SWE observations, , *33*, 9101–+, doi:10.1029/2006GL025925.

Hollweg, J. V. (1986), Transition region, corona, and solar wind in coronal holes, , *91*, 4111–4125.

Hollweg, J. V. (1999a), Kinetic Alfvén wave revisited, , *104*, 14,811–14,820, doi:10.1029/1998JA900132.

Hollweg, J. V. (1999b), Potential wells, the cyclotron resonance, and ion heating in coronal holes, , *104*, 505–520, doi:10.1029/98JA02826.

Howes, G. G., W. Dorland, S. C. Cowley, G. W. Hammett, E. Quataert, A. A. Schekochihin, and T. Tatsuno (2008b), Kinetic Simulations of Magnetized Turbulence in Astrophysical Plasmas, *Physical Review Letters*, *100*(6), 065,004–+, doi:10.1103/PhysRevLett.100.065004.

Iroshnikov, P. S. (1963), Turbulence of a Conducting Fluid in a Strong Magnetic Field, , *40*, 742–+.

Johnson, J. R., and C. Z. Cheng (2001), Stochastic ion heating at the magnetopause due to kinetic Alfvén waves, , *28*, 4421–4424, doi:10.1029/2001GL013509.

Kohl, J. L., et al. (1997), First Results from the SOHO Ultraviolet Coronagraph Spectrometer, , *175*, 613–644, doi:10.1023/A:1004903206467.

Kohl, J., et al. (1998), UVCS/SOHO empirical determinations of anisotropic velocity distributions in the solar corona, , *501*, L127, doi:10.1086/311434.

Kraichnan, R. H. (1965), Inertial-range spectrum of hydromagnetic turbulence, *Physics of Fluids*, *8*, 1385.

Kruskal, M. (1962), Asymptotic Theory of Hamiltonian and other Systems with all Solutions Nearly Periodic, *Journal of Mathematical Physics*, *3*, 806–828, doi:10.1063/1.1724285.

Lehe, R., I. J. Parrish, and E. Quataert (2009), The Heating of Test Particles in Numerical Simulations of Alfvénic Turbulence, , *707*, 404–419, doi:10.1088/0004-637X/707/1/404.

Lemaire, J., and M. Scherer (1971), Kinetic models of the solar wind., , *76*, 7479–7490, doi:10.1029/JA076i031p07479.

Li, X., S. R. Habbal, J. Kohl, and G. Noci (1998), The Effect of Temperature Anisotropy on Observations of Doppler Dimming and Pumping in the Inner Corona, , *501*, L133+, doi:10.1086/311428.

Markovskii, S. A., and J. V. Hollweg (2002), Electron heat flux instabilities in coronal holes: Implications for ion heating, , *29*, 24.

Markovskii, S. A., B. J. Vasquez, C. W. Smith, and J. V. Hollweg (2006), Dissipation of the Perpendicular Turbulent Cascade in the Solar Wind, , *639*, 1177–1185, doi: 10.1086/499398.

Marsch, E., R. Schwenn, H. Rosenbauer, K. Muehlhaeuser, W. Pilipp, and F. M. Neubauer (1982b), Solar wind protons - Three-dimensional velocity distributions and derived plasma parameters measured between 0.3 and 1 AU, , *87*, 52–72, doi: 10.1029/JA087iA01p00052.

Marsch, E., X.-Z. Ao, and C.-Y. Tu (2004), On the temperature anisotropy of the core part of the proton velocity distribution function in the solar wind, *Journal of Geophysical Research (Space Physics)*, *109*, 4102–+, doi:10.1029/2003JA010330.

Matthaeus, W. H., G. P. Zank, S. Oughton, D. J. Mullan, and P. Dmitruk (1999), Coronal heating by magnetohydrodynamic turbulence driven by reflected low-frequency waves, , *523*, L93–L96, doi:10.1086/312259.

Matthaeus, W. H., S. Servidio, and P. Dmitruk (2010), Dispersive Effects of Hall Electric Field in Turbulence, *Twelfth International Solar Wind Conference*, *1216*, 184–187, doi:10.1063/1.3395832.

McChesney, J. M., R. A. Stern, and P. M. Bellan (1987), Observation of fast stochastic ion heating by drift waves, *Physical Review Letters*, *59*, 1436–1439, doi: 10.1103/PhysRevLett.59.1436.

McComas, D. J., H. A. Elliott, N. A. Schwadron, J. T. Gosling, R. M. Skoug, and B. Goldstein (2003), The 3-D solar wind around solar maximum, in *EGS - AGU - EUG Joint Assembly*, p. 2842.

McIntosh, S. W., A. R. Davey, D. M. Hassler, J. D. Armstrong, W. Curdt, K. Wilhelm, and G. Lin (2007), Observations Supporting the Role of Magnetoconvection in Energy Supply to the Quiescent Solar Atmosphere, , *654*, 650–664, doi: 10.1086/509071.

Miralles, M. P., S. R. Cranmer, and J. L. Kohl (2002), UVCS/SOHO Observations of Large Coronal Holes During Solar Cycle 23, *AGU Fall Meeting Abstracts*, p. A451.

Miralles, M. P., S. R. Cranmer, and J. L. Kohl (2004), Low-latitude coronal holes during solar maximum, *Advances in Space Research*, *33*, 696–700, doi:10.1016/S0273-1177(03)00239-4.

Perez, J. C., and S. Boldyrev (2008), On Weak and Strong Magnetohydrodynamic Turbulence, , *672*, L61–L64, doi:10.1086/526342.

Quataert, E. (1998), Particle Heating by Alfvenic Turbulence in Hot Accretion Flows, , *500*, 978–+, doi:10.1086/305770.

Schekochihin, A. A., S. C. Cowley, W. Dorland, G. W. Hammett, G. G. Howes, E. Quataert, and T. Tatsuno (2009), Astrophysical Gyrokinetics: Kinetic and Fluid Turbulent Cascades in Magnetized Weakly Collisional Plasmas, , *182*, 310–377, doi:10.1088/0067-0049/182/1/310.

Schwadron, N. A., and D. J. McComas (2003), Solar wind scaling law, , *599*, 1395–1403, doi:10.1086/379541.

Scudder, J. D. (1992a), On the causes of temperature change in inhomogeneous low-density astrophysical plasmas, , *398*, 299–318, doi:10.1086/171858.

Scudder, J. D. (1992b), Why all stars should possess circumstellar temperature inversions, , *398*, 319–349, doi:10.1086/171859.

Shebalin, J. V., W. Matthaeus, and D. Montgomery (1983), Anisotropy in MHD turbulence due to a mean magnetic field, *Journal of Plasma Physics*, *29*, 525.

Spruit, H. C. (1981), Magnetic flux tubes, *NASA Special Publication*, *450*, 385–413.

Strauss, H. R. (1976), Nonlinear, three-dimensional magnetohydrodynamics of noncircular tokamaks, *Physics of Fluids*, *19*, 134–140, doi:10.1063/1.861310.

Tu, C., and E. Marsch (1995), MHD structures, waves and turbulence in the solar wind: Observations and theories, *Space Science Reviews*, *73*, 1–210, doi:10.1007/BF00748891.

Velli, M., R. Grappin, and A. Mangeney (1989), Turbulent cascade of incompressible unidirectional Alfven waves in the interplanetary medium, *Physical Review Letters*, *63*, 1807–1810, doi:10.1103/PhysRevLett.63.1807.

Verdini, A., and M. Velli (2007), Alfvén waves and turbulence in the solar atmosphere and solar wind, , *662*, 669–676, doi:10.1086/510710.

Wang, Y.-M., and N. R. Sheeley, Jr. (1990), Solar wind speed and coronal flux-tube expansion, , *355*, 726–732, doi:10.1086/168805.

APPENDIX

NUMERICAL METHODS & TESTS

A.1 The Temperature Profile in Coronal Holes

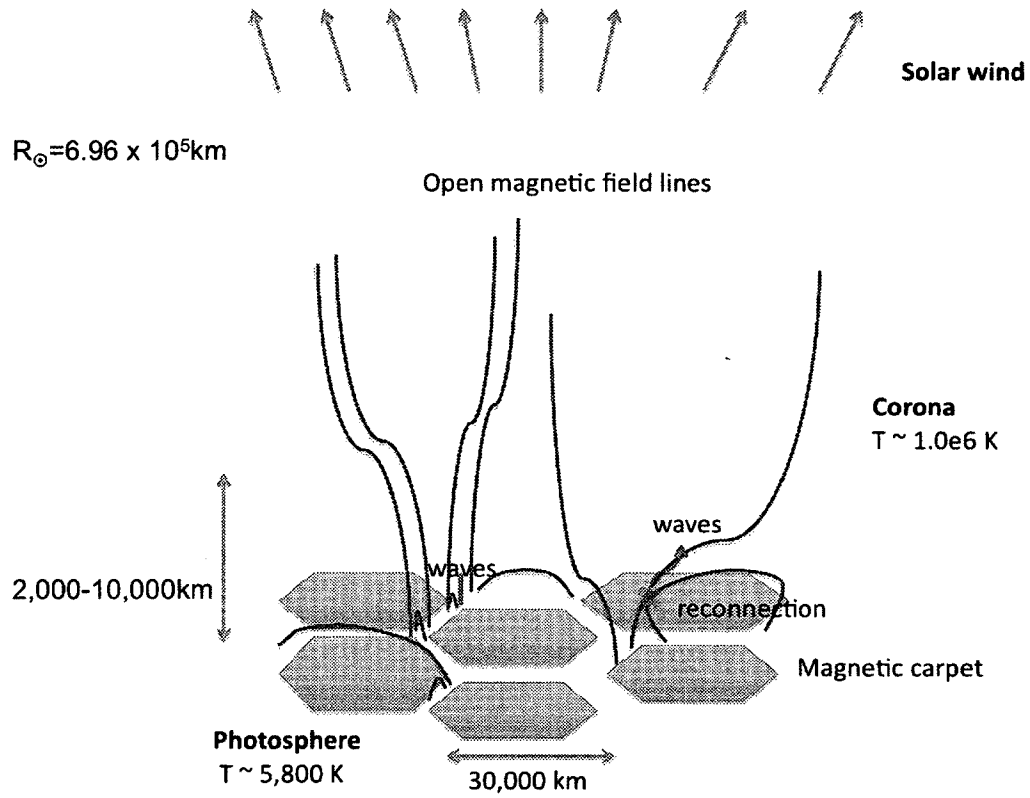

Figure A-1. Coronal holes

$R_\odot$ is the solar radius. The red lines are magnetic field lines. The blue hexagons represent supergranules. $2,000 - 10,000$km is the transition region.

A.2 The Interpolation Method

The Triangular Shaped Cloud (TSC) method is used to interpolate the value from 3 grid points. For 1D:

$$x = a_{-1} * \frac{1}{2}(\frac{1}{2} - \frac{\Delta x}{\Delta a})^2 + a_0 * (\frac{3}{4} - (\frac{\Delta x}{\Delta a})^2) + a_1 * \frac{1}{2}(\frac{1}{2} + \frac{\Delta x}{\Delta a})^2$$

where Δa is the grid length between 2 grid points, Δx is the distance away from the center of the 3 grid points. For the 4D(x,y,z,t) situation in this work, one particle needs 3^4 grid points to calculate one single component(E_i, B_i). Figure (A-2) shows the 1-D, 2-D interpolation topology.

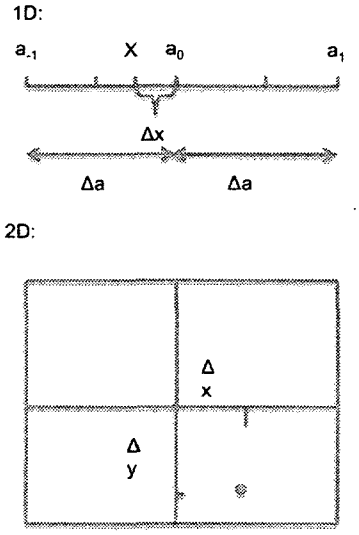

Figure A-2. Interpolation grids

These are the interpolation method behaviors in 1D and 2D. In 2D, $\Delta x/\Delta y$ is the distance between the particle's x/y position and the central point of the 9 interpolation points, which direction is uniformly at step $\Delta a_x/\Delta a_y$. $\Delta a_x = \Delta a_y$ is not required.

In the simulation, the particles could move across different CPU (or called node) domains. Here the "physical location" is used for the saving location of a particle's information, and the "real location" represents the location where the particle is in the turbulence box according to the calculated position. It may needs the grid points from different CPU to interpolate the data. In a parallel code, in order to interpolate the "real local" field, there are two ways to transfer the particles across the boundary between different nodes: CPUs communicate the boundary field between each other at every time step. When a particle moves from one node to another, the "physical location" of the particle is sent to the destined node. In this case, the "physical location" is the same as the "real location". Another way is keeping the particle's "physical location" always in the original node, and only give the particle's position to the node of the "real location", and from which the "physical" node gets the electric & magnetic field back.

The RMHD code splits the box on the $y-z$ plane, which means each node has all the x and time t data. The "real location" node interpolates along the x, t axis and leaves the rest to the "physical location" to calculate for the 4D field if we use the second method. Both methods are tested and we decide to use the last one, which performs better in our specific problems.

A.3 The Boris Pusher

In this method, the particle's position x and the local field are calculated at time $t_0, t_1, t_2, ...$, while its velocity is computed at $t_{1/2}, t_{1+1/2}, t_{2+1/2}, ...$, see Figure (A-3). At a given time $t_{n+1/2}$, the local field needed for the momentum equation is averaged from t_n and t_{n+1}.

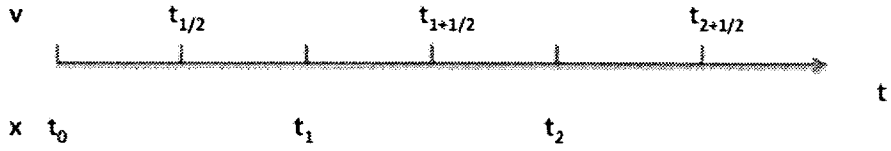

Figure A-3. The timeline of the Boris method

A.3.1 Test of Boris Pusher vs. Fourth-order Runge Kutta (RK4)

In the upper two panels of Figure (A-4), "gc1.data" is the analytical particle's trajectory in a dipolar magnetic field. "boris1.dat" and "rk3.dat" are calculated by using Boris pusher and Runge-Kutta 4th (RK4) methods. It shows that the result of Boris pusher matches better.

The bottom two panels in Figure (A-4) show the comparison of the particle's kinetic energy and magnetic moment between these two different numerical methods. In both parameters, Boris pusher shows better conservation as expected, and it takes much less calculation time than RK4.

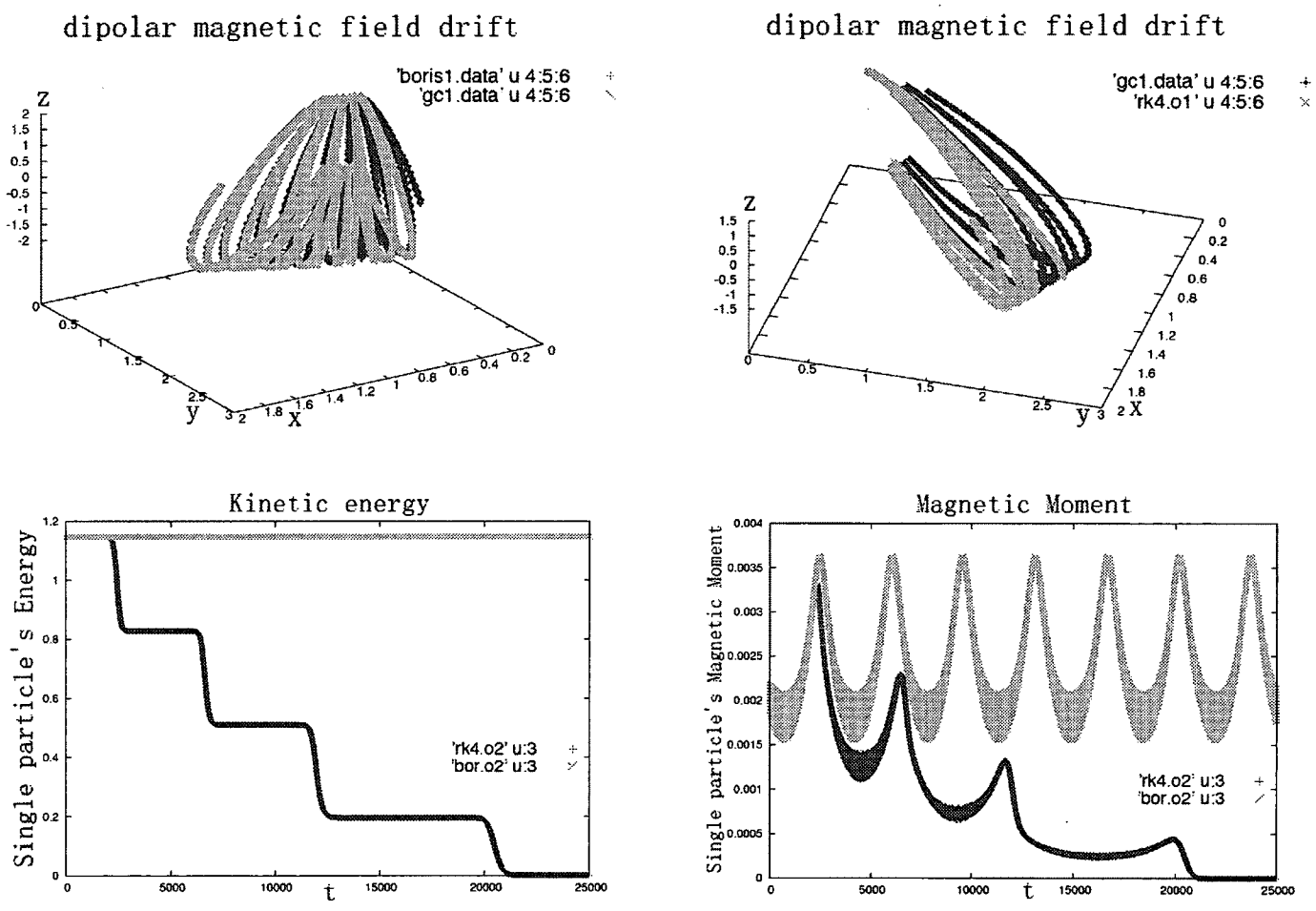

Figure A-4. Single particle in a dipolar magnetic field

A.4 Efficiency of the Method

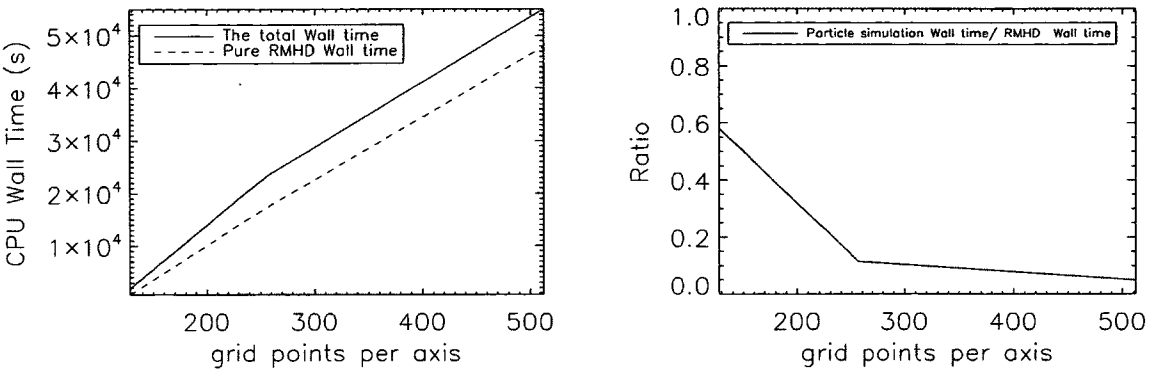

Figure A-5. Efficiency of the method

The left panel shows the CPU Wall time for 10 eddy crossing time. The right panel is the ratio of the particle simulation Wall time to the RMHD Wall time for those 10 eddy crossing time.

Here Figure (A-5) shows the particle simulation time vs the RMHD simulation cost. In those test, each CPU has 1000 particles, while we have 12 nodes are used for 128^3, 64 nodes for 256^3, and 128 nodes for $512^2 \times 256$ resolutions. The simulations only carry one specific ϵ. The comparison plots show that the test particles take much less computational times. In order to save the turbulence-field calculating time, the simulations in this work run several test particle routines with different ϵ at the same time.

A.5 Convergence Tests

A.5.1 Simulation Time

For $\epsilon = 0.06$, the heating rate $Q_\perp$ is small. If we still calculate $Q_\perp$ as what is done in Section 4.2, it would take a long CPU time to heat the particles to increase 20% energy. However, the CPU time is expensive. In this case, the temperature $< V^2 >$ already enters the stable increasing stage before the temperature hits the upper limit, as shown in the left panel of Figure (A-6). The corresponding heating rate begins to converge in the right panel of Figure (A-6), even $\Delta T < 20\% T$. So we run the simulation with small ϵ several times in a shorter time, as soon as the heating rate goes stable and convergence.

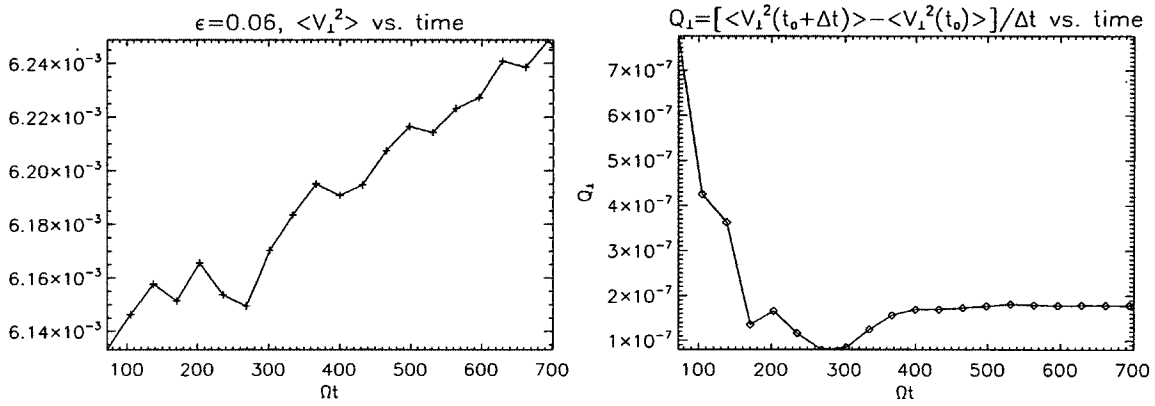

Figure A-6. The heating rate vs. time

A.5.2 Number of Test Particles

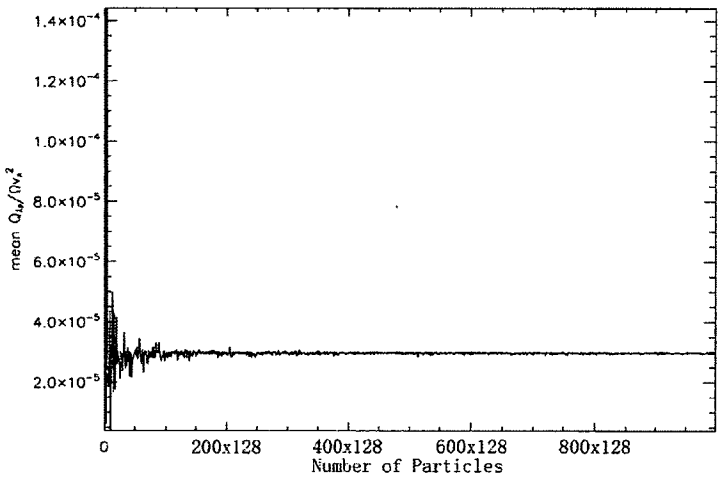

Figure A-7. Test of the reliability: Number of particles

The x axis represents how many particles are used to calculate the heating rate $Q_\perp$. The y axis shows the fluctuation amplitude of the heating rate, relative to mean value of the heating rate calculated from all the particles.

In this convergence test, the amount of particles used to calculate the heating rate for the $512^2 \times 256$ resolution simulation increases. It converges when the statistics includes more than 600×128 (128 is the number of the computation nodes) particles, even we have less than one particle in each grid box ($600 \times 128 \ll 512^2 \times 256$), see Figure (A-7).

A.5.3 Time Step

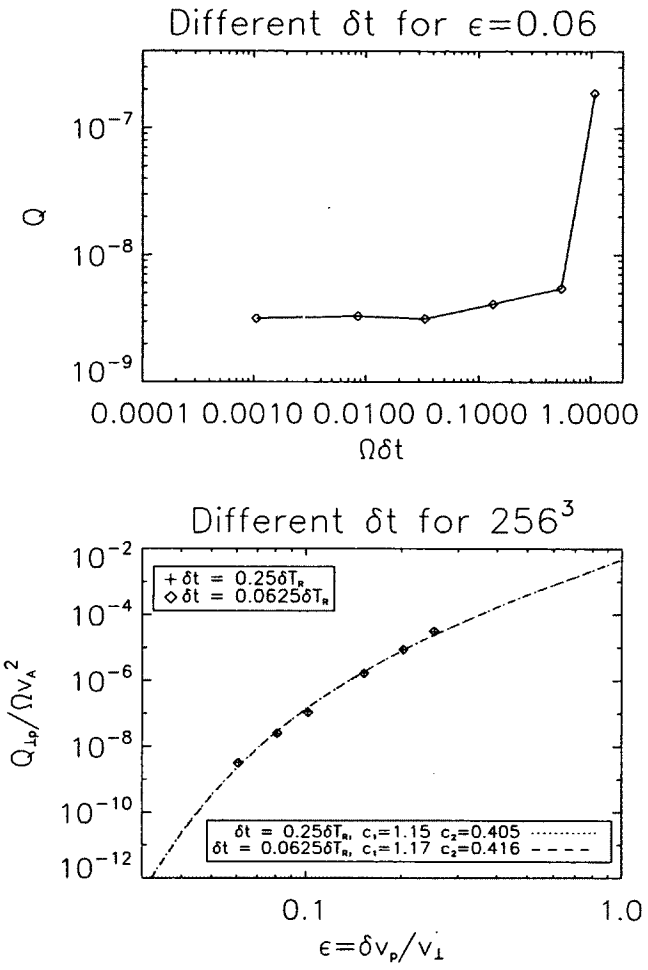

Figure A-8. Test of the reliability: Time step

In the upper panel of Figure (A-8), different time step δt is used in 256^3 simulation with normal viscosity ($p = 1$). The heating rate Q converges at $\delta t \leq 0.03\Omega^{-1}$. In the bottom panel δT_R is the time step used in the 256^3 RMHD code with $p = 1$, which is same in both runs. δt is the time step of particle tracing. $\delta T_R \sim 0.014\Omega_i^{-1}$ for $\epsilon = 0.1$. It shows that c_2 also converges for the chosen time step.

A.5.4 Different Resolutions for the Same *Re*

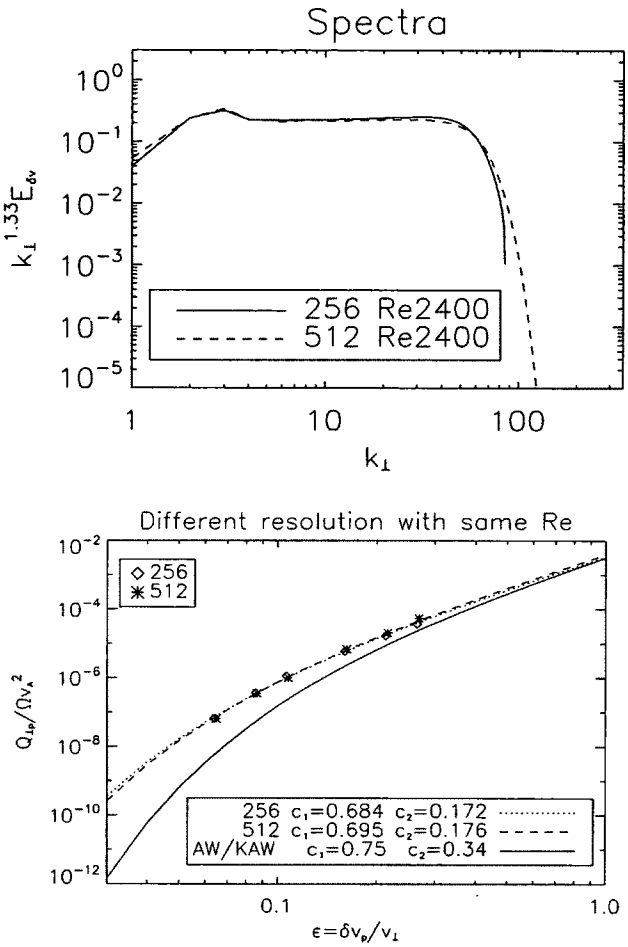

Figure A-9. Test of the reliability: $\Delta x/\rho$

The spectra in these two simulations are in the upper panel of Figure (A-9). The same viscosity is used in each $p = 4$ simulation and the spectra are very close to each other in the inertial range for different resolutions. They produce similar heating rates in the lower panel, which means that the spectrum, or the characteristics of turbulence is more important to the heating rate, rather than the resolution itself.